Dynamic induction control for mitigation of wake-induced power losses: a wind tunnel study under different inflow conditions

Manuel Alejandro Zúñiga Inestroza[1,2], Paul Hulsman[1,2], Vlaho Petrović[1,2], and Martin Kühn[1,2]

[1]Carl von Ossietzky Universität Oldenburg, School of Mathematics and Science, Institute of Physics, 26129 Oldenburg, Germany

[2]ForWind - Center for Wind Energy Research, Küpkersweg 70, 26129 Oldenburg, Germany

Correspondence: Manuel Alejandro Zúñiga Inestroza (manuel.zuniga@uni-oldenburg.de)

Abstract. Dynamic induction control (DIC), also known as the pulse method, is a wake mixing strategy that has shown promising results for mitigating wake-induced power losses in wind farms. It relies on dynamic collective blade pitching to enhance turbulent mixing, thereby accelerating the wake recovery. Experimental validation of this concept has been primarily limited to single-turbine cases under idealised conditions without shear and negligible turbulence. This paper presents a wind tunnel study to investigate the wake recovery improvement induced by DIC in single- and two-turbine configurations, as well as the potential power gains in a virtual three-turbine ~~array~~configuration. The study includes experiments under baseline uniform inflow and two realistic atmospheric boundary layer inflows. Short-range continuous-wave lidar measurements are used to remotely map the time-averaged wake characteristics of each turbine in vertical cross-sections at various downstream positions. First, the wake recovery of the upstream turbine is analysed as a function of pitch amplitude and frequency, with the latter expressed by the dimensionless Strouhal number. Next, the cascading effect of upstream turbine actuation on the wake of a downstream turbine in greedy mode is examined. Finally, wind farm power gains are assessed in a virtual three-turbine ~~setup incorporating a virtual turbine~~configuration. Compared to the baseline greedy case, improved wake recovery is observed at both the upstream and downstream turbines, solely through upstream turbine actuation across all cases. This improvement is attributed to ~~intensified turbulent mixing driven by DIC, which induces periodic thrust oscillations at both the actively controlled upstream turbine and the passive downstream turbine~~the formation of large-scale coherent structures, which excite shear layer instabilities and accelerate the onset of wake recovery. The effect is particularly pronounced at higher pitch amplitude, while differences across Strouhal number remain minor, suggesting stronger control authority through increased pitch amplitude. Despite a decrease in DIC-added wake recovery with increasing inflow turbulence, potential power gains for the wind farm persist. Overall, this study demonstrates consistent benefits and adaptability of DIC under realistic inflow conditions, highlighting its greater potential in low-turbulence environments.

1 Introduction

Wake-induced power losses and fatigue loads pose a persistent challenge for wind turbines in wind farms, with power losses exceeding 40 % under full-wake overlap conditions (Barthelmie and Jensen, 2010). This arises from the energy extraction process, which exposes downstream turbines to a wind field ~~characterised by~~ with reduced momentum and increased turbulence

(Porté-Agel et al., 2020). Although technical and economical Since technical and economic constraints make wake effects on the whole unavoidable, no control strategy is typically implemented to mitigate wake interactions between individual turbines, thereby degrading overall wind farm efficiency (Boersma et al., 2017). To address this, largely unavoidable, advanced wind farm flow control strategies are being developed to minimise mitigate wake losses and ultimately reduce the levelised cost of energy (Meyers et al., 2022). These strategies often involve turbine-level actuation (e.g. yaw , or pitch) based on optimal control setpoints , which improve the inflow conditions at to improve inflow conditions for downstream turbines (Houck, 2022). Consequently, When effectively implemented, this can benefit overall plant performance can benefit through increased power production or reduced fatigue loads. Although first commercial solutions are emerging, widespread adoption remains limited, requiring further research and development.

Typically, wind farm flow control implementation focuses foremost on wind farm power maximisation (van Wingerden et al., 2020). To this end, research has primarily centred on wake steering and static induction control strategies (Kheirabadi and Nagamune, 2019). Wake steering involves intentionally yawing upstream turbines to deflect their wakes away from downstream turbines, thereby increasing the total power output (Fleming et al., 2015; Hulsman et al., 2024). This concept has received the most attention and development, but challenges remain due to the strong dependence of optimal setpoints on temporal variations in wind direction (Dallas et al., 2024) and power loss behaviour (Howland et al., 2020; Hulsman et al., 2022a). On the other hand, static induction control involves derating upstream turbines through pitch control, torque control, or a combination of both to reduce their wake deficit and increase the energy available to downstream turbines (Houck, 2022). Inconsistent simulation results have undermined interest in this concept. However, power gains may still be achievable under partial wake conditions or with closely spaced turbines (van der Hoek et al., 2019; Zúñiga Inestroza et al., 2024).

Wake mixing strategies based on individual or collective pitching have demonstrated potential for increased wind farm power production (Meyers et al., 2022). Unlike wake steering and static induction control, these techniques aim to actively excite wake instabilities, promoting enhanced turbulent mixing and accelerating wake recovery (Houck, 2022). The collective-pitch-based approach, commonly termed dynamic induction control (DIC) or the pulse method, is the focus of this study and its literature review. First results from large-eddy simulations (LES) report power gains of up to $16\,\%$ (Goit and Meyers, 2015) and $7\,\%$ (Goit et al., 2016) in a 10×5 wind farm with and without entrance effects, respectively. However, these studies used a computationally expensive optimisation approach that yielded impractical control signals. Building on this, Munters and Meyers (2018) introduced a simplified method based on sinusoidal thrust variations to mimic the periodic shedding of vortex rings observed previously by Goit and Meyers (2015). This approach provided power gains of up to $5\,\%$ in a 4×4 wind farm, decreasing to approximately $2\,\%$ at higher inflow turbulence. Yılmaz and Meyers (2018) further advanced this by synthesising a periodic signal based on optimal generator torque and pitch control, achieving power gains of up to $25\,\%$ in a two-turbine setup configuration under uniform inflow in LES. These gains diminished or even disappeared with increasing turbulence intensity and integral length scale.

Unfortunately, experimental validation of DIC is currently limited to a few wind tunnel studies. Frederik et al. (2020b) report power gains of up to $4\,\%$ in a three-turbine setup configuration under two different atmospheric boundary layer (ABL) inflows. Combining wind tunnel experiments with numerical simulations, Wang et al. (2020) indicate maximum power gains of $3.6\,\%$

in a three-turbine array with 5 % inflow turbulence intensity. Based on particle image velocimetry measurements, van der Hoek et al. (2022) demonstrate improved wake recovery due to DIC applied to a single turbine under uniform inflow. Although no power gains were achieved in a virtual two-turbine configuration, subsequent results with a second physical turbine showed a gain of 0.6 % (van der Hoek et al., 2024).

While initial numerical and experimental investigations into DIC show promising results, several knowledge gaps remain open regarding the performance of DIC parameters under different inflow and operating conditions, including the level of wake recovery improvement, achievable wind farm power gains, cascading effects on downstream turbines, the physical mechanisms behind DIC and ABL flow interactions, the impact on fatigue loads, among others. Further validation through wind tunnel experiments is essential to bridge the gap between numerical simulations and currently absent field tests, offering well-controlled and repeatable conditions. This paper presents a wind tunnel study to investigate the wake recovery improvement and wind farm power gains induced by DIC under baseline uniform inflow and two realistic ABL inflows. Specifically, the following aspects are addressed:

1. exploring the wake recovery improvement as a function of pitch amplitude and frequency;
2. examining the cascading effect of upstream turbine actuation on a downstream turbine and its wake;
3. evaluating the potential wind farm power gains in a virtual three-turbine ~~array~~configuration.

The ~~rest~~ remainder of the paper is ~~organised~~ structured as follows: Sect. 2 outlines the experimental methodology, Sect. 3 presents the results, Sect. 4 ~~provides an analysis and discussion~~discusses the experimental findings, and Sect. 5 ~~summarises the key conclusions~~ provides the concluding remarks of the study.

2 Methodology

This section outlines the experimental methodology. Section 2.1 introduces the wind tunnel facility and the active grid used to generate ABL inflows. Section 2.2 describes the model wind turbine, while Sect. 2.3 explains the greedy and DIC ~~control strategies~~operating modes. Section 2.4 details the flow measurement techniques, including a short-range continuous-wave lidar and complementary ~~hot wire~~ hot-wire measurements. Finally, Sect. 2.5 provides an overview of the experimental setup and measurement ~~cases~~procedure.

2.1 Wind tunnel facility

The experiments ~~were~~ are carried out in the large wind tunnel at ForWind, University of Oldenburg, Germany. It is a Göttingen-type wind tunnel with a contraction ratio of 4:1, a cross-section of $3\,\mathrm{m} \times 3\,\mathrm{m}$ and a closed test section length of $30\,\mathrm{m}$. It consists of five $6\,\mathrm{m}$ long movable segments, allowing operation in open, partially open or closed test section configuration. The airflow is driven by four $110\,\mathrm{kW}$ fans capable of reaching wind speeds of up to $42\,\mathrm{m\,s^{-1}}$ with turbulence intensity levels below 0.2 % when no active grid is installed. A cooling system is used to maintain a constant temperature during operation, while the roof of each test section segment is adjusted to achieve a zero pressure gradient. An active grid can be installed at the wind tunnel nozzle to generate tailored, reproducible turbulent and sheared inflows. The active grid consists of 80 shafts with square flaps, which can be independently controlled to modify the local blockage of the flow. This is achieved by dynamically varying the angle of the flaps according to user-defined motion protocols (Kröger et al., 2018; Neuhaus et al., 2021).

2.2 Model wind turbine

Two in-house developed MoWiTO 0.6 model wind turbines ~~were~~ are used during the measurement campaign. The rotor blades are designed according to the NREL–5 MW reference turbine (Jonkman et al., 2009), with a geometric scaling factor of 1:217, resulting in a rotor diameter of 0.58 m and a blockage ratio below 3 % in the wind tunnel. To account for scaling effects and manufacturing constraints, the blades feature an SD7003 low-Reynolds-number ~~airfoil (Schottler et al., 2016).~~ (Re) airfoil with increased chord length and tailored twist distribution along the span (Schottler et al., 2016). While this improves aerodynamic performance in the operating low-Re regimes typical of wind tunnel testing, the power coefficient (C_P) remains unavoidably lower than that of full-scale turbines (Wang et al., 2021). The nacelle houses a direct current (DC) motor (Faulhaber 3863H048CR) acting as a generator and a stepper motor (Faulhaber AM2224-R3-4.8-36) used for collective blade pitching, both equipped with an encoder. The DC motor's encoder measures the rotational speed (rpm), while the aerodynamic torque is estimated from the voltage drop across a shunt resistor. The stepper motor's encoder measures the collective blade pitch angle. These values are then used to calculate the electrical power generated by the model wind turbine. Additionally, a field-effect transistor acts as a variable resistor within the circuit, enabling control of the generator torque for rotor speed adjustment. Furthermore, the tower base is instrumented with strain gauges (HBM 1-DY43-3/350) in full Wheatstone bridge configuration to obtain thrust measurements. Calibration is done by hanging known weights on the nacelle's rear through a pulley system at the start of the measuring campaign. All control algorithms (e.g. torque control, pitch control) are executed in real-time on a National Instruments cRIO-9066 system, while acquiring the data at 5 kHz.

2.3 Control strategies

Two different control modes ~~were~~ are implemented during the experiments: (i) baseline greedy control and (ii) DIC.

2.3.1 Greedy mode

The greedy control mode follows the conventional $K\omega^2$ control law by Bossanyi (2000), which aims to maximise the turbine's power output in the partial load region. This is achieved by setting the generator torque (Q_G) proportional to the square of the rotor speed (ω), as follows:

$$Q_\mathrm{G} = K\omega^2 = \frac{\rho\pi R^5 C_\mathrm{Q}(\lambda^*,\beta^*)}{2\lambda^{*2}}\omega^2, \tag{1}$$

where K is the controller gain, depending on the air density (ρ), rotor radius (R), torque coefficient (C_Q) and design tip speed ratio (λ^*). C_Q is a function of both λ^* and the optimal pitch angle (β^*). The generator torque is adjusted via a proportional-integral-derivative (PID) controlled external voltage, which ensures the rotor speed is maintained at the point of optimal efficiency. MoWiTO 0.6 uses a ~~set-point~~ setpoint function $Q_\mathrm{G}(\omega)$ derived from characterisation experiments conducted at various wind speeds and pitch angles at the start of each measurement campaign. For this campaign, the turbines operated optimally at a tip speed ratio λ = 5.60, thrust coefficient C_T = 0.86 and power coefficient C_P = 0.37, at an inflow wind speed of $7\,\mathrm{m\,s^{-1}}$.

2.3.2 DIC mode

The DIC mode applies a sinusoidal signal to the collective blade pitch controller to induce periodic thrust oscillations, while the baseline generator torque controller remains active to maintain operation near optimal aerodynamic efficiency. Although pitch actuation causes fluctuations and a reduced mean in C_Q, the controller gain K is not updated during the experiments. The control signal to the stepper motor is parameterised by the pitch excitation amplitude (A) and frequency (f_β), the latter typically expressed in terms of the dimensionless Strouhal number (St). Here, St represents the ratio of the flow oscillation speed due to periodic pitching to the convective flow speed, defined as:

$$St = \frac{f_\beta D}{u_\infty}, \tag{2}$$

where D is the rotor diameter, and u_∞ is the average inflow wind speed at hub height. The dynamic collective blade pitching ($\hat{\beta}$) is then described by:

$$\hat{\beta} = \beta_0 + A \sin\left(2\pi \frac{St\, u_\infty}{D} t\right), \tag{3}$$

where β_0 is the fine pitch angle that maximises power in the partial-load region, and t is the time. The range of St for this study is chosen based on previous numerical (Munters and Meyers, 2018; Yılmaz and Meyers, 2018) and experimental studies (Frederik et al., 2020b; Wang et al., 2020), which report optimal wake recovery within ~~$St \in [0.24, 0.38]$~~ $St \in [0.24, 0.38]$. Figure 1a illustrates the collective blade pitch signal under both greedy and DIC modes. The DIC signal is implemented at $u_\infty = 7\,\mathrm{m\,s^{-1}}$, with ~~$A = 2°$ and $St = 0.30$~~ $A = 2°$ and $St = 0.30$ (i.e. $f_\beta = 3.63\,\mathrm{Hz}$). This corresponds to a low-frequency actuation of about $0.017\,\mathrm{Hz}$ at the NREL–5 MW scale, with one cycle completed every $59\,\mathrm{s}$. Figure 1b depicts the C_T for both control modes, with the DIC case showing a clear harmonic response to the sinusoidal pitch actuation.

2.4 Flow measurements

2.4.1 WindScanner lidar

Wake measurements ~~were~~ are performed with a short-range continuous-wave WindScanner lidar, developed and manufactured by the Technical University of Denmark (DTU). This remote sensing device provides highly spatially resolved flow measurements over large measurement planes in a flexible manner, without flow disturbance. Its effectiveness has been demonstrated in previous wind tunnel experiments combined with model wind turbines (e.g., van Dooren et al., 2017; Hulsman et al., 2020, 2022b; Zúñiga Inestroza et al., 2024), showing good agreement with hot-wire measurements to capture the main trends of average streamwise velocity field and dissipation rate of turbulence in wind turbine wakes. It is equipped with a steerable scan head, driven by two prism motors and a focus motor, enabling precise focus point adjustments. This allows for measurements in both staring and scanning modes, following user-defined trajectories. The WindScanner uses a coherent detection

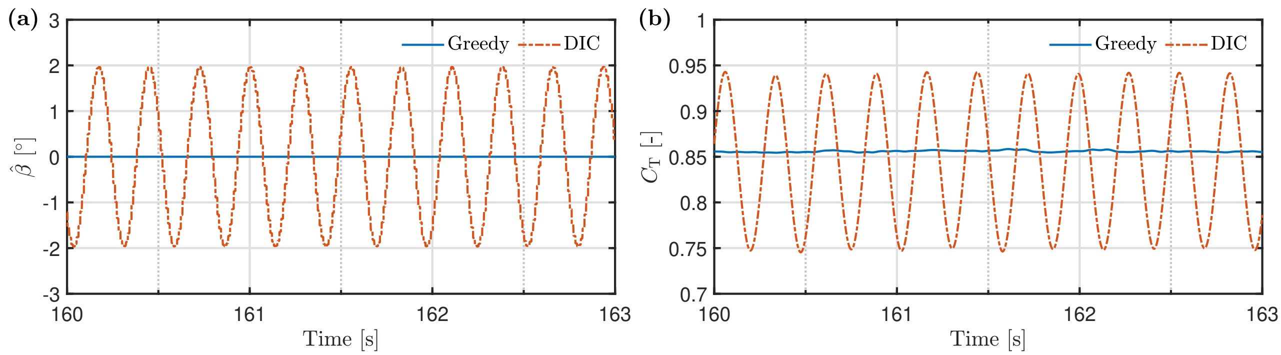

Figure 1. Time series excerpt depicting: (a) the collective blade pitch signal and (b) the thrust coefficient under greedy and DIC (~~$St = 0.30, A = 2°$~~$St = 0.30, A = 2°$) operation modes.

method to determine the Doppler frequency shift in the backscattered signal of a focused laser beam within a probe volume. At the start of each measurement campaign, the focus point is calibrated by determining the lidar's location and orientation relative to the experimental setup using a Leica total station. Additionally, an infrared detector card is used to verify the commanded measurement points. Further details on the use and setup of WindScanners in wind tunnel experiments can be found in (van Dooren et al., 2017; Hulsman et al., 2022b).

In this study, a single WindScanner ~~was~~ is used to retrieve the local streamwise velocity component (u) of the wind velocity vector at a sampling rate of $451.7\,\mathrm{Hz}$. This approach neglects the lateral (v) and vertical (w) components, potentially introducing relative errors of up to $2.4\,\%$ ~~(Hulsman et al., 2022b).~~ (cf. uncertainty analysis of single-Doppler reconstruction in

~~width=0.65Figs/f02a.pngtrim=1cm 2.6cm 20cm 3.2cm,clip,~~

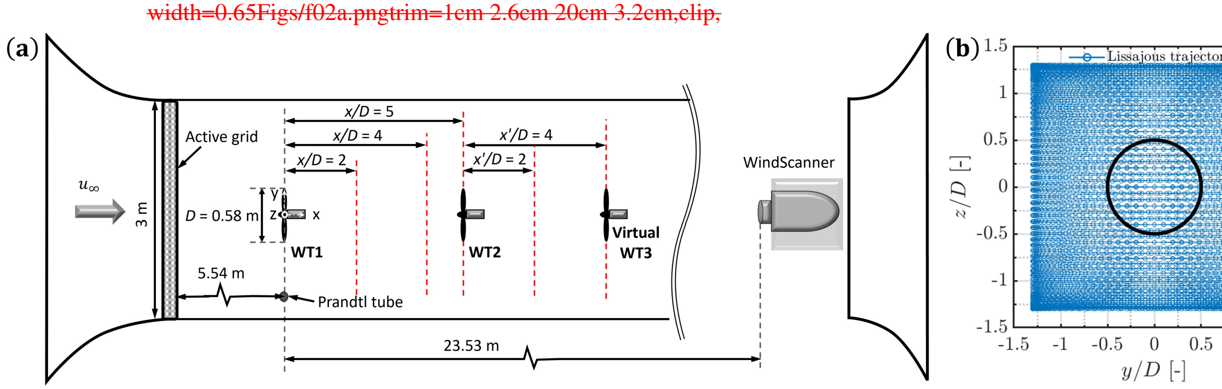

~~scale=0.46Figs/f02b.eps~~

Figure 2. (a) Top-view schematic of the experimental setup (not to scale), detailing the arrangement of the model wind turbines and the wake measurement positions (red dahsed lines). (b) Lissajous scanning trajectory used by the WindScanner to map the wake in vertical cross-sections at each downstream location.

Appendix A1). Taking this into account, u can be derived according to:

$$u = \frac{1}{\cos\chi\cos\delta}\frac{1}{\cos\phi\cos\theta}\left(v_{\mathrm{LOS}} - v\sin\chi\cos\delta\sin\phi\cos\theta - w\sin\delta\sin\theta\right) \approx \frac{v_{\mathrm{LOS}}}{\cos\chi\cos\delta}\frac{v_{\mathrm{LOS}}}{\cos\phi\cos\theta}, \quad (4)$$

where v_{LOS} is the measured line-of-sight wind speed along the laser's beam direction, ~~χ and δ~~ ϕ and θ are the azimuth and elevation angles of the line-of-sight direction, respectively.

During the measurement campaign, the WindScanner ~~was~~ is used to obtain time-averaged wake characteristics in vertical cross-sections at downstream distances ~~$x/D \in \{2,4,5,7,9\}$~~$x/D \in \{2,4,5,7,9\}$. The coordinate system is defined at the rotor centre of the first turbine, where x, y and z are the longitudinal, transversal, and vertical directions, respectively. Figure 2a provides a schematic of the experimental setup (described in Sect. 2.5), with red dashed lines indicating the wake measurement positions. Each vertical scan ~~followed~~ follows a Lissajous scanning trajectory comprising of 5000 points (Figure 2b), with a period of 15 s per scan. The scanning process ~~was~~ is repeated for 10 min per case, resulting in over 40 scans per vertical plane at every downstream distance. Postprocessing of the data ~~included~~ includes interpolation and averaging onto a grid with 0.13 D by 0.13 D cells~~, resulting in at least~~ . This yields approximately 300 data points ~~per grid cell~~ at the central grid cell at hub height, and considerably higher measurement density near the boundaries of the scanning area, consistent with the Lissajous trajectory.

2.4.2 Hot-wire array

An important limitation when using WindScanner measurements in a wind tunnel is the probe volume averaging effect, which limits the accuracy of turbulence estimates. Since the laser focuses on a thin cylindrical volume rather than an infinitesimal point, turbulent structures with a length scale smaller than the probe volume length are partially filtered out (Uluocak et al., 2024). Therefore, complementary hot-wire measurements ~~were~~ are conducted for a limited number of cases under uniform inflow, providing insights into the ~~impact of DIC on wake-added turbulence~~ turbulence development in the wake of a DIC actuated turbine compared to the greedy case. The array ~~consisted~~ consists of 19 one-dimensional hot wires mounted on an aluminium structure in a horizontal line at hub height~~. This covered~~ , spanning over a range of ~~$y/D \in [-1.25, 1.25]$~~$y/D \in [-1.25, 1.25]$. A traverse system ~~facilitated~~ facilitates the measurement of horizontal wake profiles at ~~$x/D \in \{2,3,5\}$~~$x/D \in \{2,3,5\}$. Two Dantec Dynamics 54N80 multi-channel Constant Temperature Anemometry (CTA) systems ~~were~~ are used to sample data at 6 kHz over a period of 120 s. Calibration ~~was~~ is done before and after the measurements against a Prandtl tube positioned approximately 2 m in front of the traversing structure.

2.5 Experimental setup and measurement procedure

The experimental setup involved a wind tunnel configuration with a partially open test section, ~~consisting of~~ comprising four connected segments with a total length of 24 m. The last segment was removed to ~~install the WindScanner~~accommodate the WindScanner, installed on a steel platform near the diffuser, ~~along with~~ alongside a PALAS AGF 10.0 seeding generator to ~~ensure~~ provide adequate aerosol circulation for laser backscattering. The ~~measurement campaign comprised experiments with~~

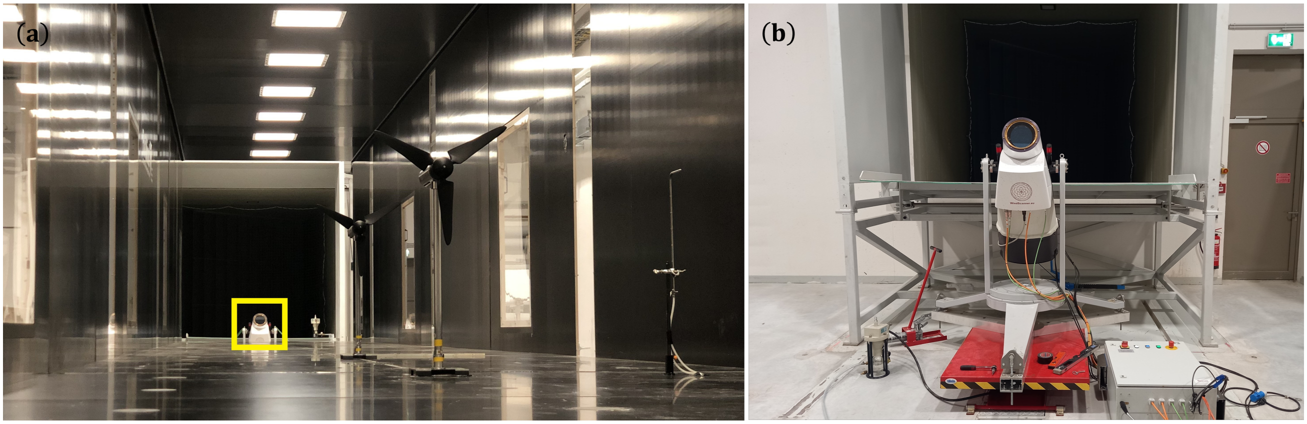

Figure 3. (a) Upstream view of the experimental setup with two MoWiTO 0.6 and the WindScanner (yellow square). (b) Close-up of the WindScanner lidar used to remotely map the wake.

inflow wind speed was monitored with a Prandtl tube positioned perpendicular to the upstream turbine's rotor plane at hub height, $0.9\,\mathrm{m}$ to the left of the tunnel centreline.

The measurement campaign included experiments in both single- and two-turbine configurations. ~~For the~~ Figure 3a shows an upstream view of the two-turbine configuration, while Fig. 3b highlights the installation of the WindScanner. In the single-turbine ~~setup~~configuration, the first turbine (WT1) was positioned $9.55\,D$ $(5.54\,\mathrm{m})$ from the nozzle ~~at~~ on the tunnel centreline. This configuration ~~allowed~~ aimed to investigate the dependence of wake recovery on pitch amplitude and Strouhal number. Specifically, the time-averaged wake response of WT1 was examined with the WindScanner ~~under DIC mode for~~ at downstream positions $x/D \in \{2,4,5\}$, under both greedy and DIC operation modes. For the DIC cases, pitch frequencies corresponding to ~~$St \in \{0.25, 0.30, 0.40\}$, each at amplitudes of $A \in \{1°, 2°\}$, and compared to the greedy control case at $x/D \in \{2,4,5\}$. For~~ $St \in \{0.25, 0.30, 0.40\}$ and amplitudes $A \in \{1°, 2°\}$ were considered.

In the two-turbine ~~setup~~configuration, a second turbine (WT2) was installed $5\,D$ $(2.9\,\mathrm{m})$ downstream of WT1. ~~The focus here was on examining the cascading effects~~ Here, the focus was on the cascading effect of WT1 actuation on ~~the wake of~~ WT2. ~~Thus~~To this end, the wake of WT2 was examined ~~with the WindScanner for the same DIC cases applied~~ in response to WT1 ~~and compared against the greedy case at $x/D \in \{7,9\}$, which corresponds to $x'/D \in \{2,4\}$, with $x'/D = 0$ defined relative to the position of~~ operating in greedy and DIC modes, while WT2 ~~. Note that WT2~~ remained in greedy ~~operation throughoutthe experiments. The inflow wind speed was monitored with a Prandtl tube perpendiculat to WT1's rotor plane at hub height and positioned to the left of the tunnel centreline. Figure 3a provides an upstream view of the two-turbine setup, while Fig. 3b highlights the installation of the WindScanner~~mode throughout. For each case, the wake of WT2 was mapped with the WindScanner at downstream positions $x'/D \in \{2,4\}$, with $x'/D = 0$ defined relative to the position of WT2.

All experiments were conducted in the partial load region at $u_\infty = (7.0 \pm 0.1)\,\mathrm{m\,s^{-1}}$ ~~for~~, resulting in a rotor-based Reynolds number of $Re \approx 2.9 \times 10^5$. Although lower than that of full-scale turbines, typically $\mathcal{O}(10^6)$ to $\mathcal{O}(10^7)$, Chamorro et al. (2012) suggest Re independence of the main wake statistics for rotor-based $Re > 9.3 \times 10^4$. The campaign encompassed three differ-

Table 1. Development of turbulence intensity (TI) along the wind tunnel test section at hub height for different inflow conditions, measured using hot wires (HW) or WindScanner staring mode (WS).

Inflow	$x/D=0$	$x/D=2$	$x/D=5$	$x/D=7$	$x/D=9$	
Uniform (HW)	0.2	0.2	0.2	0.2	0.2	[%]
ABL Type-I (WS)	3.8	3.9	4.0	4.0	4.1	[%]
ABL Type-II (WS)	8.4	7.8	7.5	7.2	7.0	[%]

ent inflow conditions: (i) uniform (no shear), (ii) ABL Type-I ($\alpha = 0.11$), and (iii) ABL Type-II ($\alpha = 0.22$), where α represents the best-fit power law exponent accounting for wind shear across the rotor area. The active grid was installed at the nozzle and used in active mode to generate the ABL inflows, while no grid (empty nozzle) was used for the uniform inflow. The WindScanner was used to characterise the inflow development along the empty test section at $x/D \in \{0,2,5,7,9\}$. The vertical profiles of normalised wind speed (u/u_∞) for all three inflow conditions are shown in Fig. 4. Note that $x/D = 9$ is excluded for the uniform inflow case due to a faulty data set. Each point represent the spatially averaged streamwise velocity component across all horizontal positions (y/D) at each height (z/D). Despite slight variations for the ABL cases, the wind speed distribution remained fairly stable along the test section for all inflow cases. The inflow turbulence intensity (TI) was measured along the tunnel centreline at hub height using the WindScanner's staring mode for both ABL cases, while hot-wire measurements were used for the uniform inflow case. Note that the measured TI using the WindScanner is inherently low-pass filtered due to probe-volume averaging effects, as explained in Sect. 2.4.2. Table 1 summarises the TI values for all inflows at $x/D \in \{0,2,5,7,9\}$. The stability of the flow throughout the measurement domain is corroborated under uniform inflow, with an average TI of $0.2\,\%$. For ABL Type-I, TI shows slight downstream variations, while for ABL Type-II, it decays as expected for fully developed flows behind a grid. Given the reproducibility of the inflows generated by the active grid, all experiments are expected to have experienced similar TI variations without compromising the validity of the results.

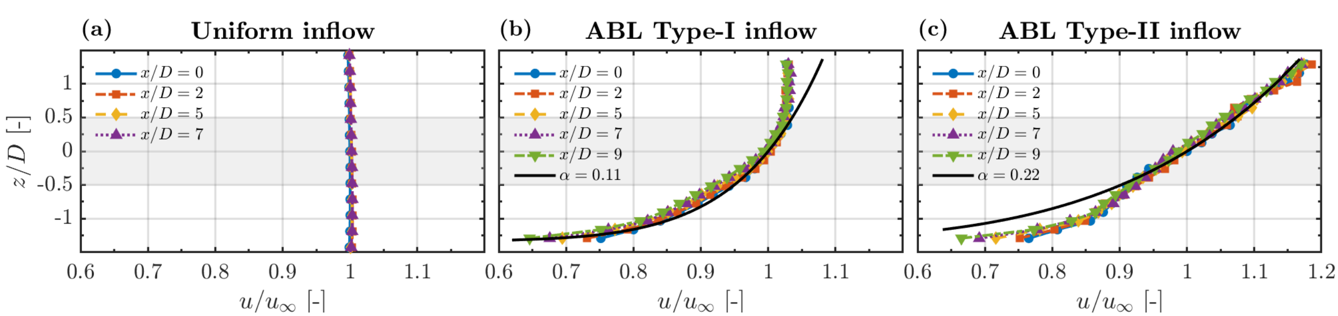

Figure 4. Vertical profiles of normalised wind speed (u/u_∞) measured by the WindScanner along the empty wind tunnel test section for different inflow conditions. The grey shaded region represents the rotor area.

3 Results

The experimental results are organised into three main sections. Section 3.1 focuses on the single-turbine ~~setup~~configuration, analysing the impact of WT1 actuation on wake recovery improvement, ~~wake-added turbulence~~ wake turbulence development, and thrust coefficient behaviour. Section 3.2 centres on the two-turbine ~~setup~~configuration, exploring the cascading ~~effects~~ effect of WT1 actuation on WT2's wake recovery and thrust coefficient. Section 3.3 evaluates the potential wind farm power gains in a virtual three-turbine ~~setup, utilising a virtual turbine in the analysis~~configuration.

3.1 Single-turbine ~~setup~~configuration: impact of pitch actuation amplitude and Strouhal number

3.1.1 Wake recovery ~~improvement~~ of WT1

The impact of WT1 pitch actuation with DIC on wake recovery is analysed in terms of pitch amplitude and Strouhal number relative to the greedy case across different inflow conditions. ~~Figure 5 illustrates this by presenting~~ To illustrate this, Fig. 5 presents wake contours of the normalised streamwise velocity difference between DIC and the baseline greedy case $(u_{\mathrm{DIC}} - u_{\mathrm{Greedy}})/u_\infty$. Each row corresponds to a distinct inflow type, with each subfigure depicting a different downstream position, ~~$x/D \in \{2,4,5\}$~~$x/D \in \{2,4,5\}$. Two pitch amplitudes, ~~$A \in \{1°,2°\}$~~$A \in \{1°,2°\}$, are examined under uniform inflow (Fig. 5~~a-f~~a–f), while only $A = 2°$ is ~~investigated~~ considered under both ABL inflows (Fig. 5~~g-l). Since~~ g–l), as it yielded stronger wake recovery under baseline uniform inflow. Also, since similar trends are observed for different Strouhal numbers (cf. wind speed deficit profiles of WT1 at hub height in Appendix ~~A1~~B1), only ~~cases with~~ results from WT1 actuation at $St = 0.30$ are ~~depicted here. Time-averaged wake contours of WT1 depicting the normalised streamwise velocity difference between DIC at $St = 0.30$ and the baseline greedy case $(u_{\mathrm{DIC}} - u_{\mathrm{Greedy}})/u_\infty$. Each row represents a different inflow condition at downstream locations $x/D \in \{2,4,5\}$. The black circumference outlines the edges of a virtual downstream turbine. The wake is visualised from the WindScanner perspective, looking upstream towards WT1 with a clockwise wake rotation.~~ displayed.

~~At~~ In general, at $x/D = 2$, DIC ~~results in~~ induces a wind speed deficit (blue regions) at the wake centre and the surrounding flow, while increasing the ~~available~~ wind speed in an annulus near the rotor edges (red ~~region).~~ regions). This corresponds to an accelerated transition from a double- to a single-Gaussian wake profile. Further downstream, at ~~$x/D \in \{4,5\}$, this~~ $x/D \in \{4,5\}$, the annulus gradually expands to encompass almost the entire swept area of a virtual turbine (indicated by ~~a~~ the black circumference), with the magnitude of increased wind speed also rising, especially ~~at the higher amplitude of~~ for DIC cases with higher amplitude ($A = 2°$). Additionally, the wind speed deficit in the surrounding flow becomes more pronounced, concentrating in a semiannular-shaped region above hub height, indicating predominant momentum entrainment from aloft. These patterns are consistent under both uniform and ABL Type-I inflow conditions, although the ~~ABL case exhibits more pronounced~~ wind speed deficit patches ~~, particularly in the upper region of the velocity field, due to the inflow wind shear. For the~~ are slightly more pronounced for the ABL case. This can be attributed to the enhanced vertical momentum entrainment triggered by DIC (Brown et al., 2025), which represents a dominant mechanism for energy replenishment in the wake of turbines interacting with boundary layer inflows (Cal et al., 2010).

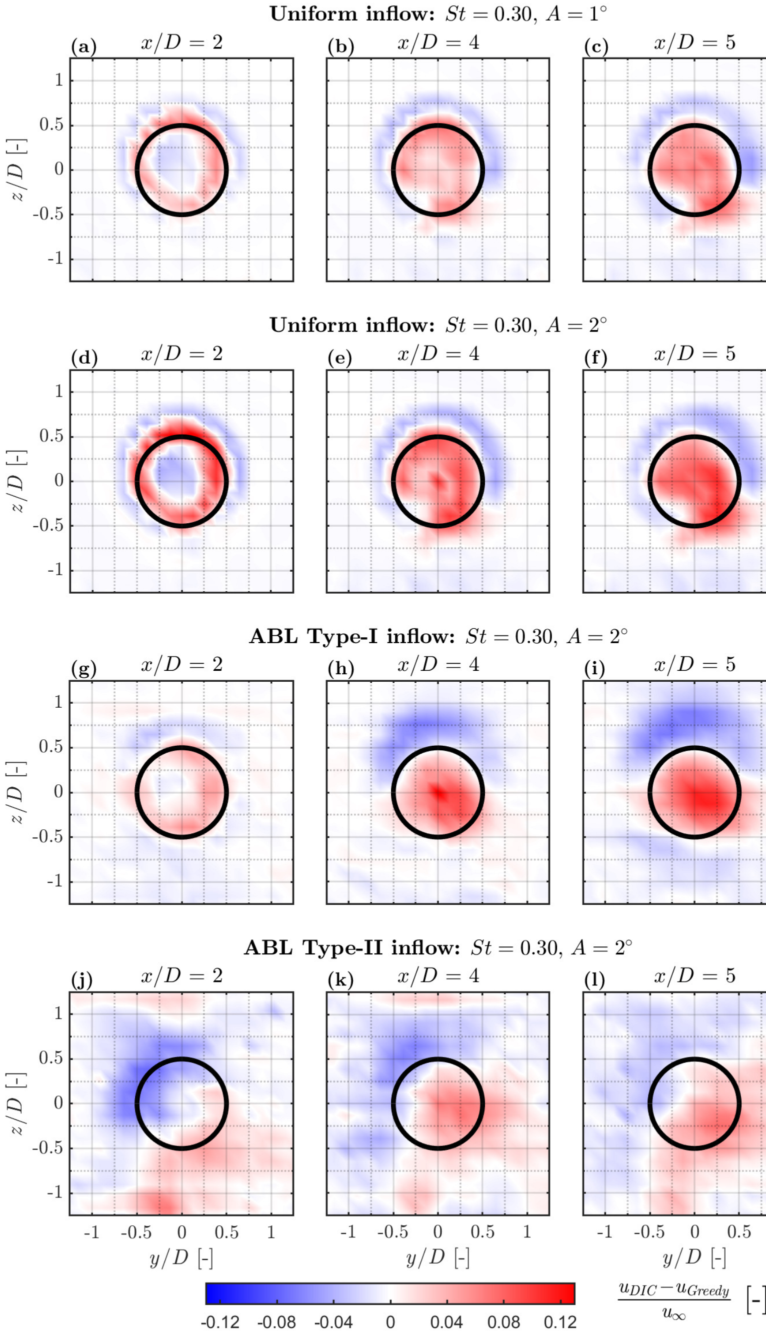

Figure 5. Time-averaged wake contours of WT1 depicting the normalised streamwise velocity difference between operation under DIC mode at $St = 0.30$ and the baseline greedy mode $(u_{\mathrm{DIC}} - u_{\mathrm{Greedy}})/u_\infty$. Each row represents a different inflow condition at downstream locations $x/D \in \{2, 4, 5\}$. The black circumference outlines the edges of a virtual downstream turbine. The counter-rotating wake is shown from the WindScanner perspective, looking upstream towards WT1, thus perceived as a clockwise rotation.

Comparatively, under ABL Type-II inflow, ~~DIC causes~~ the wake re-energisation induced by WT1 actuation exhibits a markedly asymmetric distribution~~of relative changes in the wake velocity field. At~~. Specifically, at $x/D = 2$, the wind speed deficit is concentrated in the second quadrant, while patches of increased wind speed appear in the ~~fourth. The quadrants~~ third and fourth. Quadrants are defined counterclockwise from the positive x-axis, following standard mathematical convention. This asymmetry may be linked to the development of nacelle- and tower-induced turbulence, which is enhanced by DIC (van der Hoek et al., 2022). Since wake TI below hub height is typically reduced under strongly sheared ABL inflow (Porté-Agel et al., 2020), their relative contribution may explain the observed pattern. Further downstream, at $x/D \in \{4,5\}$, the wind speed deficit diffuses more into the surrounding flow compared to previous cases, while regions of higher wind speed spread across the rotor area, remaining predominantly deflected to the right. ~~Potential causes of this asymmetric wake behaviour are discussed in Sect. 4.~~ This asymmetric behaviour can be partly attributed to the effect of wake rotation under sheared inflow conditions, which causes high-momentum flow from aloft to be transported downward and low-momentum near the ground upward (Gebraad et al., 2016). Consequently, the wake of a turbine operating in greedy mode deflects slightly to the right when viewed upstream (Fleming et al., 2014). This effect is particularly pronounced under highly sheared and turbulent inflow but appears to be disrupted by DIC. In fact, analysis of the wake centre revealed reduced lateral deflection across all DIC cases under ABL inflow. This finding aligns with Brown et al. (2025), who similarly observed that DIC reduces wake skew under sheared and veered inflow conditions.

To quantify the wake recovery improvement ~~due to~~ from WT1 actuation, Fig. 6 presents bar charts of the normalised rotor equivalent wind speed ($u_{\mathrm{REWS}}/u_\infty$) ~~as a function of downstream distance is computed~~ for WT1 operating under greedy and DIC modes, assuming a full-wake overlap scenario~~(Fig. 6).~~. Each subchart corresponds to a different inflow ~~type~~condition, with groups of four bars comparing ~~greedy and DIC cases~~ the two modes at downstream positions ~~$x/D \in \{2,4,5\}$. The~~ $x/D \in \{2,4,5\}$. The u_{REWS} method provides a weighted average wind speed ~~provides a better estimate of the energy available in the wake, which could be captured by a downstream turbine. For this purpose, the wake within the~~ across the rotor swept area, accounting for spatial variations in the velocity field (Wagner et al., 2011). In this study, the rotor area is ~~divided~~ segmented into five ring segments based on the measured wake cross-sections, as follows:

$$u_{\mathrm{REWS}} = \sqrt[3]{\sum_{i=1}^{5} u_i^3 \frac{A_i}{A_{\mathrm{R}}}}, \tag{5}$$

where u_i is the average wind speed within the i-th ring segment, A_i is the area of the i-th ring segment, and A_{R} is the rotor swept area. Since the outer rings cover a larger area, they are weighted more heavily and contribute more to the energy that would be captured by a virtual downstream turbine, neglecting tip-losses. Percentage values indicate the relative change in $u_{\mathrm{REWS}}/u_\infty$ ~~due to DIC compared to the greedy case, with~~ with respect to the baseline greedy case. Red arrows alongside bold text highlighting the optimal recovery~~. The red~~, while the grey error bars indicate the rotor average uncertainty of $u_{\mathrm{REWS}}/u_\infty$, calculated according to the standard uncertainty propagation method used in (van Dooren et al., 2017; Hulsman et al., 2022b).

Experiments under uniform inflow reveal a dependence of wake recovery on pitch amplitude and Strouhal number. For $A = 1°$, the optimal wake recovery relative to the greedy case occurs at the highest frequency tested ($St = 0.40$) across all

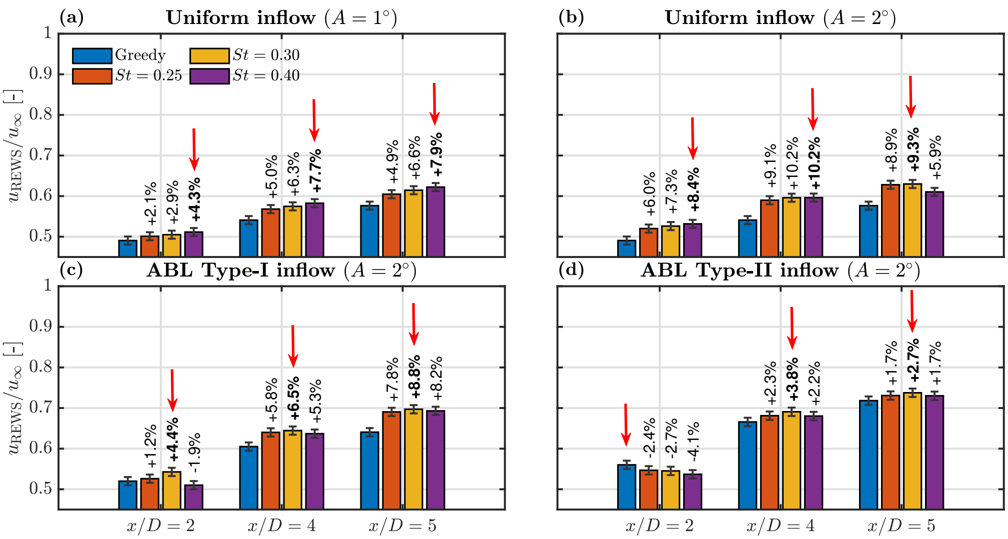

Figure 6. Wake recovery of WT1 expressed by the normalised rotor equivalent wind speed ($u_{\mathrm{REWS}}/u_\infty$). Each subchart corresponds to a different inflow ~~type~~condition, with groups of four bars comparing results from WT1 operating in greedy and DIC ~~cases~~ modes at downstream positions ~~$x/D \in \{2,4,5\}$~~ $x/D \in \{2,4,5\}$. Percentage values indicate the relative change ~~in $u_{\mathrm{REWS}}/u_\infty$ due~~ with respect to ~~DIC compared to~~ the baseline greedy case. ~~Bold~~ Red arrows alongside bold text ~~highlights~~ highlight the optimal recovery.

downstream positions, reaching a peak of 7.9 % at $x/D = 5$. In comparison, for $A = 2°$, the optimal St varies with downstream distance: $St = 0.40$ at $x/D = 2$, a similar recovery for $St \in \{0.30, 0.40\}$ at $x/D = 4$, and $St = 0.30$ at $x/D = 5$. The highest recovery (10.2 %) is achieved at $x/D = 4$. Noteworthy is that the magnitude of wake recovery improvement is more responsive to increased amplitude than to changes in Strouhal number. For ABL Type-I inflow, the optimal recovery consistently aligns with $St = 0.30$ at all downstream distances, with a maximum improvement of 8.8 % at $x/D = 5$. For ABL Type-II inflow, the optimal recovery is also achieved with $St = 0.30$, reaching a peak of 3.8 % at $x/D = 4$, while no benefit is attained at $x/D = 2$ due to the asymmetry described earlier.

3.1.2 ~~DIC-added turbulence~~ Turbulence development in the wake of WT1

~~To analyse the impact of DIC on added turbulence relative to the baseline greedy case~~ To better understand the improved wake recovery observed when DIC mode is active, the turbulence development in the wake of WT1 is analysed under uniform inflow conditions for selected DIC cases in comparison to the greedy case. As a first metric, Fig. 7 presents horizontal wake profiles of the local turbulence intensity (TI) at hub height for downstream distances ~~$x/D \in \{2,3,5\}$ under uniform inflow conditions~~ $x/D \in \{2,3,5\}$. These profiles provide indication ~~of the~~ on the level of wind speed fluctuations within the wake, ~~derived~~ computed with the local time series from hot-wire measurements as follows:

$$TI(y) = \frac{\sigma(y)}{< u(y) >} \frac{\sigma(y)}{\langle u(y) \rangle}, \quad (6)$$

where $\sigma(y)$ is the local standard deviation and $<u(y)>$ $\langle u(y)\rangle$ is the local mean wind speed, both as functions of the transversal position y. The top row illustrates the effect of increasing Strouhal number $St \in \{0.25, 0.30\}$ at $A = 2°$, while the bottom row shows the effect of increasing amplitude $A \in \{1°, 2°\}$ at $St = 0.30$. Compared Remarkably, compared to the greedy operationmode, all DIC cases display exhibit a significant increase in local turbulence and an earlier transition to the far wake far-wake region. The latter is typically characterised distinguished by the merging of the TI profile into a single peak at the wake centre. Note that the differences in local TI among DIC cases with increasing Strouhal numbers at , resulting from shear layer expansion following the breakdown of tip vortices, which otherwise inhibit momentum exchange with the surrounding flow (Lignarolo et al., 2015; Porté-Agel et al., 2020). Once this occurs, the far-wake is said to be reached, which gradually transitions into fully developed decaying turbulence (i.e. homogeneous isotropic turbulence) before eventually recovering to undisturbed conditions (Neunaber et al., 2020). Moreover, when looking at the effect of increasing Strouhal number $St \in \{0.25, 0.30\}$ with the same amplitude are marginal (Fig. 7a-c). Conversely, the increase in local TI is more pronounced for DIC cases with higher amplitude at the same Strouhal number (Fig. 7d-f). Likewise, the $A = 2°$, the resulting differences in local TI are marginal. Conversely, increasing the amplitude from $A = 1°$ to $A = 2°$ while keeping the same $St = 0.30$ leads to a more pronounced increase in TI, while also exhibiting an earlier transition to the far wake region occurs more rapidly with $A = 2°$ compared to the case with $A = 1°$, as indicated by the single peak TI profile, along with a far-wake. This is evidenced by the local maximum around $x/D = 3$ at the wake centre for $A = 2°$. Further downstream, at $x/D = 5$, TI is already decaying for the DIC cases, whereas for the greedy case, the merging has not yet occurred and instead the local TI is still building up.

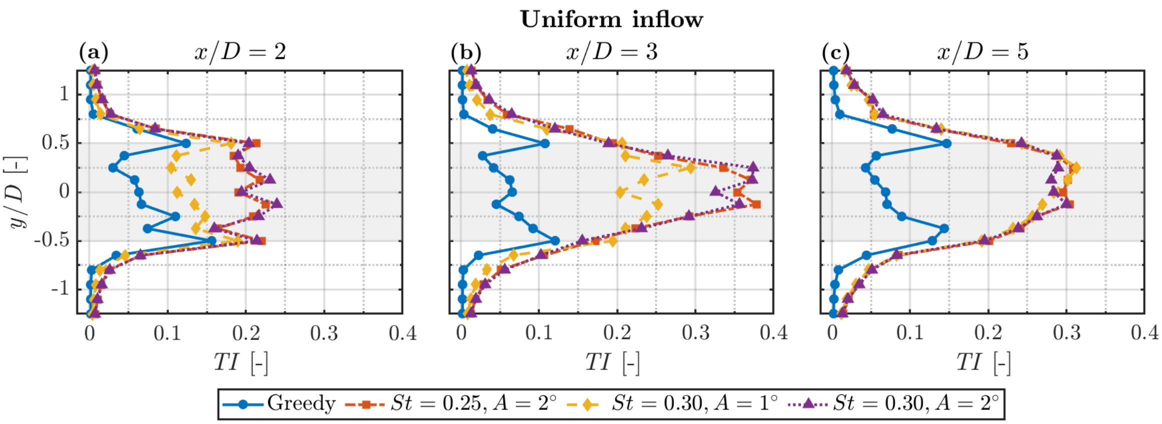

Figure 7. Horizontal wake profiles Downstream evolution of WT1 showing local turbulence intensity (TI) profiles in the wake of WT1 at hub height under uniform inflow conditions. The top row Each subfigure compares the effect of increasing Strouhal number at a fixed amplitude of $A = 2°$ with the baseline greedy case , while the bottom row depicts the impact of increasing amplitude with different DIC cases at downstream locations $x/D \in \{2, 3, 5\}$. Shaded grey regions indicate the same Strouhal number of $St = 0.30$rotor swept area.

As a second metric, Fig. 8 compares the downstream evolution of the local power spectra $\phi_{u'}$ along the wake centreline $y/D = 0$ for the greedy case and two DIC cases with the same $St = 0.30$ but different amplitude. This provides insight into the wake energy distribution across different turbulence scales, as well as the presence of coherent structures. The power spectra are computed with the standard Welch's algorithm in MATLAB (2024), using the local time series of the wind speed fluctuations, $u'(y) = u(y) - \langle u(y) \rangle$. The frequency axis is expressed in terms of the dimensionless Strouhal number. In general, the energy content remains largely unchanged across all downstream locations for the baseline greedy case, consistent with the slow turbulence build up observed in the local TI profiles. On the other hand, the DIC cases exhibit not only higher energy spectra but also distinct peaks at the frequency of pitch actuation $St = 0.30$ and its higher harmonics. This indicates the presence of large-scale coherent structures, which can be associated with the emergence of vortex rings, as reported in (Munters and Meyers, 2018; Yılmaz and Meyers, 2018). In fact, Yılmaz and Meyers (2018) show that these structures cause an earlier wake breakdown, enhancing the momentum entrainment into the wake core. Furthermore, looking at the spectra of different amplitude cases, the convergence to a single spectrum with similar energy across all frequencies by $x/D = 3$ indicates an earlier transition to the far-wake region for the high amplitude case ($A = 2°$). The zoomed-in view of the dominant peak at $St = 0.30$ confirms that a turbulence plateau is reached at $x/D = 3$, followed by a decay at $x/D = 5$. In contrast, the low-amplitude case ($A = 1°$) exhibits a slower turbulence build-up, with the highest energy content observed at $x/D = 5$. Additionally, although not shown here, spectral analysis of the shear layer region at the rotor edges reveals an even more rapid turbulence development for both amplitude cases. This is reasonable since the transition to the far-wake region starts with the breakdown of the helical tip-vortex system into small-scale turbulence structures (Lignarolo et al., 2015) but also results in the formation of vortex rings due to periodic flow disturbances induced by DIC. This fuels momentum transport towards the wake core in response to a faster shear layer expansion.

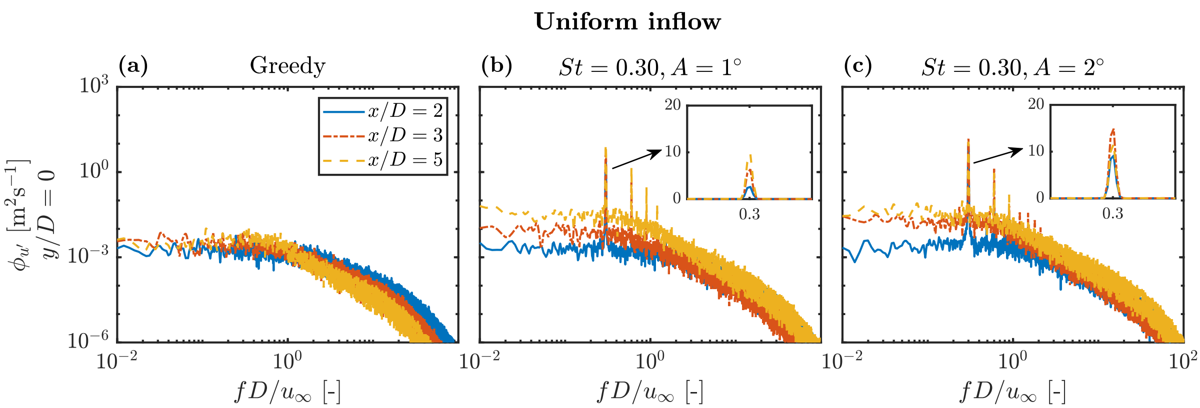

Figure 8. Downstream evolution of the local power spectra of wind speed fluctuations ($\phi_{u'}$) at the wake centreline ($y/D = 0$) of WT1 under uniform inflow conditions. For DIC cases, zoomed insets illustrate the downstream development of the dominant coherent structure at $St = 0.30$.

3.1.3 Thrust coefficient of WT1

To qualitatively illustrate the periodic C_{T} oscillations induced by collective blade pitchingthrust oscillations ($C_{\mathrm{T,WT1}}$) induced by WT1 pitch actuation, Fig. 8a–c 9 presents time series excerpts under of WT1 operating in greedy and DIC ($St = 0.30$) operation modes across different inflow conditions. For comparisoneach case, the time series are synchronised to analyse the turbine behaviour when exposed to the same varying identical inflow conditions. Additionally, the raw signals are low-pass filtered at 12 Hz to remove high-frequency noise . Here, C_{T} is calculated according to: and facilitate visualisation. To prevent phase distortion, a sixth-order Butterworth filter is applied using the `filtfilt` function in MATLAB (2024). $C_{\mathrm{T,WT1}}$ is then calculated as follows:

$$C_{\mathrm{T}\,\mathrm{T,WT1}} = \frac{F_{\mathrm{T}}}{0.5\rho\pi R^2 u_\infty^2}\,\frac{F_{\mathrm{T,WT1}}}{0.5\rho\pi R^2 u_\infty^2}, \tag{7}$$

where F_{T} $F_{\mathrm{T,WT1}}$ is the instantaneous thrust force measured via strain gauges at the tower base of WT1, ρ is the average air density, R is the rotor radius, and u_∞ is a 10 min averaged wind speed measured by the Prandtl tube at hub height. Note that in cases with ABL inflow for cases under ABL inflow conditions, this point measurement does not fully represent inflow variations across the rotor area. In general, DIC is effectively translated into periodic periodic oscillations of C_{T} Nevertheless, it is observed that DIC effectively induces periodic $C_{\mathrm{T,WT1}}$ oscillations across all inflow conditions. To quantify these variations, Table 2 summarises the mean C_{T} statistical trends in the mean and standard deviation of WT1, averaged over $C_{\mathrm{T,WT1}}$ across all cases. The reported values represent 10 min for each case and inflow condition, with the standard deviation shown in parentheses next to the mean value. Compared to the greedy case, the relative change in mean C_{T} across different St casesis marginal at $A = 1°$ under uniform inflow, while a slight decrease is observed for DIC cases with $A = 2°$. Notably, averages, obtained after low-pass filtering the data at 250 Hz. This choice filters out high-frequency noise while preserving most relevant dynamic components. Further increases in the standard deviation becomes more pronounced with increasing amplitude. With negligible TI under uniform inflow, the standard deviation relative to the greedy case increases drastically by approximately at $A = 1°$ and at $A = 2°$. For experiments under both ABL inflow types, the mean C_{T} is moderately higher for all DIC cases, being most pronounced at $St = 0.40$. The sheared and turbulent nature of ABL inflows results in higher standard deviation for

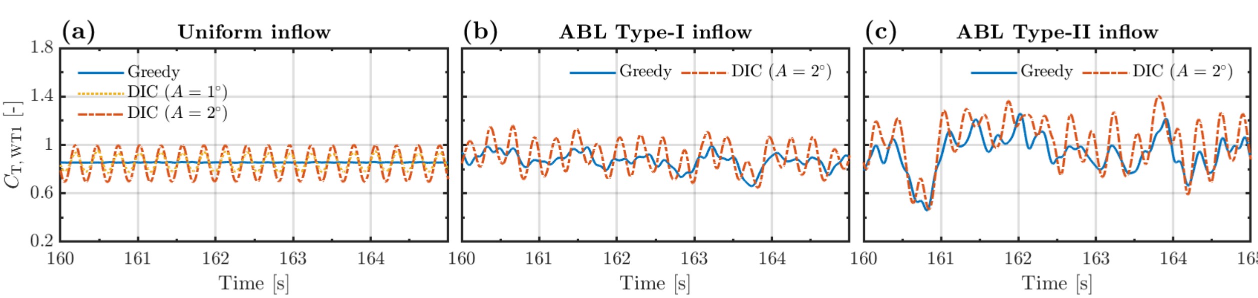

Figure 9. Time series excerpts comparing WT1's thrust coefficient ($C_{\mathrm{T,WT1}}$) under greedy and DIC ($St = 0.30$) operation modes across different inflow conditions.

the baseline greedy case, reducing the relative variation increase for DIC cases to for ABL Type-I and for ABL Type-IIcut-off frequency resulted in negligible variations.

Table 2. Time series excerpts depicting WT1's thrust coefficient Statistical trends in the mean and standard deviation ($C_T$in parentheses) of $C_{T,WT1}$ under greedy and DIC ($St = 0.30$) operation operating modes across different inflow conditions.

Mean thrust coefficient (C_T) of WT1 for greedy and DIC cases across different inflow conditions, with standard deviation in parentheses.

	Uniform inflow				ABL Type-I		ABL Type-II	
St [-]	$A = 1°$		$A = 2°$		$A = 2°$		$A = 2°$	
Greedy	0.86	(0.010.02)	0.86	(0.010.02)	0.88	(0.080.11)	0.91	(0.150.22)
0.25	0.86	(0.060.07)	0.84	(0.100.12)	0.90	(0.130.15)	0.93	(0.200.25)
0.30	0.86	(0.060.08)	0.84	(0.100.14)	0.92	(0.130.17)	0.93	(0.200.26)
0.40	0.85	(0.060.11)	0.84	(0.100.19)	0.93	(0.120.20)	0.95	(0.200.27)

Under uniform inflow, the mean $C_{T,WT1}$ remains nearly constant across St cases at low pitch amplitude ($A = 1°$), while a slight decrease occurs at higher amplitude ($A = 2°$). By comparison, DIC markedly increases the standard deviation of $C_{T,WT1}$ across all actuated cases. Given the negligible inflow TI, the relative increase over the greedy case peaks at $450\,\%$ for $A = 1°$ and $850\,\%$ for $A = 2°$, both at $St = 0.40$. Moreover, at low amplitude, optimal recovery aligns with $St = 0.40$, corresponding to the highest fluctuation energy in $C_{T,WT1}$. In contrast, at higher amplitude, optimal recovery initially aligns with $St = 0.40$ earlier downstream but shifts to $St = 0.30$ further downstream, despite this not corresponding to the highest standard deviation (see Fig. 6). Comparatively, experiments under ABL inflow show a moderately higher mean $C_{T,WT1}$ even in the baseline greedy case, particularly for the strongly sheared ABL Type-II. This is attributed to the vertical shear, which shifts the wind centre of pressure (i.e. the point where the resultant wind force acts) above hub height due to higher momentum in the upper half of the rotor. Also, since DIC induces periodic thrust oscillations, its interaction with sheared inflow likely causes a shift in the thrust load centre. This leads to an increase in mean $C_{T,WT1}$ with increasing St, being most pronounced at $St = 0.40$ due to more energetic fluctuations, as reflected by the higher standard deviation. Nevertheless, it is worth noting that optimal recovery aligns with $St = 0.30$ under both ABL inflows (Fig. 6), despite this not corresponding to the highest fluctuation energy in $C_{T,WT1}$. Furthermore, the sheared and turbulent nature of ABL inflows yields a higher baseline standard deviation, thereby reducing the relative increase in DIC-induced fluctuations up to $82\,\%$ for ABL Type-I and $23\,\%$ for ABL Type-II. Overall, these observations indicate that optimal St depends not only on the magnitude of induced thrust fluctuations but also on the interaction between actuation amplitude, inflow turbulence and wake evolution.

3.2 Two-turbine setupconfiguration: cascading effects effect of upstream turbine actuation on a downstream turbine

3.2.1 Wake recovery improvement of WT2

~~Time-averaged wake contours of WT2 depicting the normalised streamwise velocity difference between cases with and without WT1 actuation $(u_{\mathrm{DIC}} - u_{\mathrm{Greedy}})/u_{\infty}$. Each row corresponds to a different inflow condition at downstream locations $x'/D \in \{2,4\}$, with $x'/D = 0$ defined relative to the position of WT2. The black circumference outlines the edges of a virtual downstream turbine. The wake is visualised from the WindScanner perspective, looking upstream towards WT2 with a clockwise wake rotation. WT2 remains in greedy operation throughout.~~

~~To investigate the cascading effects~~ To illustrate the cascading effect of WT1 ~~actuation via DIC~~ pitch actuation on WT2's wake recovery, Fig. ~~9 shows~~ 10 presents wake contours of the normalised streamwise velocity difference ~~between cases with and without WT1 actuation~~ $(u_{\mathrm{DIC}} - u_{\mathrm{Greedy}})/u_{\infty}$ resulting from WT1 operating in DIC and greedy modes, while WT2 remains in greedy mode. Each row corresponds to a distinct inflow condition, ~~and each subfigure represents specific downstream locations $x'/D \in \{2,4\}$, where $x'/D = 0$ is defined relative to the position of WT2. Note that WT2 operates in greedy mode across all cases. Since similar~~ with each subfigure depicting a different downstream location $x'/D \in \{2,4\}$. Since similar cascading trends are observed across ~~different Strouhal numbers~~ all St cases (cf. wind speed deficit profiles of WT2 at hub height in Appendix ~~??~~B2), only ~~cases with~~ results from WT1 actuation at $St = 0.30$ are ~~presented here.~~ displayed.

In general, WT1 actuation consistently enhances ~~the wake recovery of~~ WT2's wake recovery across all inflow conditions. Notably, the wake ~~exhibits regions of increased available~~ contours exhibit patches of increased wind speed (red regions) spanning ~~almost~~ nearly the entire rotor area of a virtual downstream turbine~~. This area extends to the right, while~~, concurrently surrounded by wind speed deficit patches (blue regions) ~~in the upper and lower regions. These patterns are consistent across all DIC~~ above and below. A slight extension of the high-speed region towards the right-hand side, beyond the rotor area, is also observed, likely due to wake rotation effects. These patterns indicate enhanced turbulent entrainment in WT2's wake as a result of WT1 actuation, which not only improves recovery of its own wake but also induces thrust oscillations at WT2, as described in Sect. 3.2.2. The cascading effects are present across all St cases, becoming slightly more pronounced at higher amplitude ($A = 2°$~~. Under~~). Furthermore, under ABL inflow, the ~~effects remain visible but are more diffused for the~~ overall patterns persist but appear more diffuse for ABL Type-II~~inflow.~~. This is due to the impact of higher ambient turbulence and a concurrent reduction in cascading fluctuations at WT2.

To quantify the wake recovery improvement of WT2, Fig. ~~10~~ 11 presents bar charts of the normalised rotor equivalent wind speed ($u_{\mathrm{REWS}}/u_{\infty}$) at downstream distances ~~$x'/D \in \{2,4\}$~~$x'/D \in \{2,4\}$. Each subchart corresponds to a distinct inflow ~~type~~condition, with groups of four bars comparing ~~cases with and without~~ results from WT1 ~~actuation~~operating in greedy and DIC modes, while WT2 remain in greedy mode. Under uniform inflow, the magnitude of wake recovery improves with increasing amplitude and downstream distance, ~~peaking at~~ reaching optimal gains with $St = 0.30$ ~~and~~ at $x'/D = 4$~~, with a~~. Specifically, a relative increase of 10.3 % ~~at~~ for $A = 1°$ and 11.9 % ~~at~~ for $A = 2°$ ~~. A similar trend is~~ is observed. The alignment with $St = 0.30$ for both amplitudes is attributed to the higher turbulence levels in WT2's wake, which promote faster wake recovery even without WT1 actuation. Interestingly, the improvement in WT2's wake recovery due to WT1 actuation is similar to, or even exceeds, that of WT1's wake. This is related to the higher turbulence in WT2's wake, as well as to the fact that the energy content of the induced thrust oscillations at WT2 remains comparable to that of the actuated WT1, as described in Sect. 3.2.2. Furthermore, similar trends are observed under ABL ~~Type-I inflow, though~~ inflow, albeit with slightly

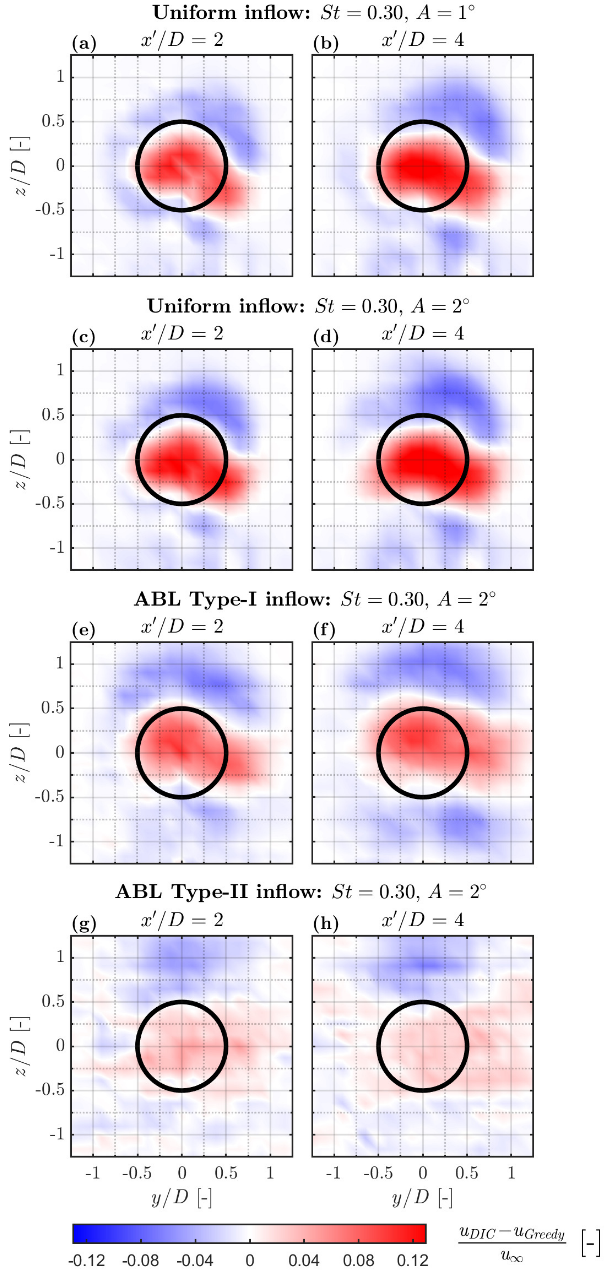

Figure 10. Time-averaged wake contours of WT2 depicting the normalised streamwise velocity difference $(u_{\mathrm{DIC}} - u_{\mathrm{Greedy}})/u_\infty$ resulting from WT1 operating in DIC and greedy modes, while WT2 remains in greedy mode. Each row corresponds to a different inflow condition at downstream locations $x'/D \in \{2, 4\}$, with $x'/D = 0$ defined relative to the position of WT2. The black circumference outlines the edges of a virtual downstream turbine. The counter-rotating wake is visualised from the WindScanner perspective, looking upstream towards WT2, thus perceived as a clockwise rotation.

smaller ~~improvement, reaching a maximum of . For the~~ improvements, as the increased ambient turbulence reduces cascading fluctuations at WT2. For ABL Type-I, the relative increase peaks at 8.9 % with $St = 0.30$ at $x'/D = 2$, then decreases to 8.1 % at $x'/D = 4$. For ABL Type-II~~inflow~~, the wake recovery improvement is further reduced, reaching a maximum of 3.7 % with $St = 0.30$ at $x'/D = 2$ and 2.5 % with $St = 0.25$ at $x'/D = 4$.

3.2.2 Thrust coefficient of WT2

~~The cascading effects~~ In this section, the cascading effect of WT1 pitch actuation on WT2 ~~are analysed here~~ is analysed in terms of ~~thrust variations and average~~induced thrust fluctuations. Fig. ~~11 displays C_T~~ 12 compares time series excerpts of WT2~~, comparing cases with ($St = 0.30$) and without~~'s thrust coefficient ($C_{\mathrm{T,WT2}}$) resulting from WT1 ~~actuation~~ operating in greedy and DIC ($St = 0.30$) modes across different inflow conditions~~. Compared to the greedy case, the C_T~~, while WT2 remains in greedy mode. $C_{\mathrm{T,WT2}}$ is calculated similarly to WT1, as follows:

$$C_{\mathrm{T,WT2}} = \frac{F_{\mathrm{T,WT2}}}{0.5\rho\pi R^2 u_\infty^2}, \tag{8}$$

where $F_{\mathrm{T,W2}}$ is the instantaneous thrust force measured via strain gauges at the tower base of WT2~~exhibits~~. In general, $C_{\mathrm{T,WT2}}$ exhibits clear periodic fluctuations in response to ~~the harmonic actuation of WT1. To quantify these variations,~~ WT1's harmonic pitch actuation, which results in periodic excitation of the flow impinging on WT2. Notably, the induced $C_{\mathrm{T,WT2}}$

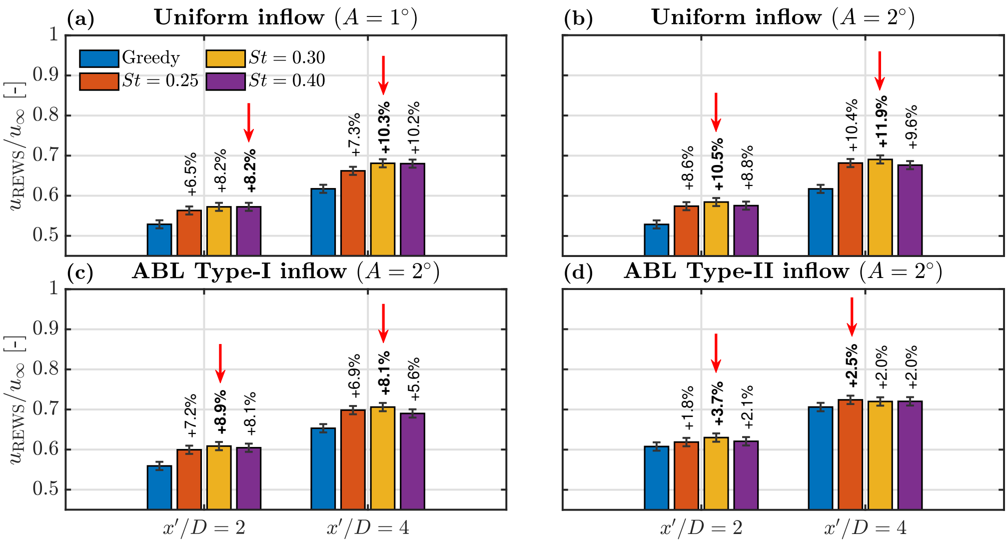

Figure 11. Wake recovery of WT2 expressed by the normalised rotor equivalent wind speed ($u_{\mathrm{REWS}}/u_\infty$) at downstream positions ~~$x'/D \in \{2,4\}$~~$x'/D \in \{2,4\}$, with $x'/D = 0$ defined relative to the position of WT2. Each subchart corresponds to a different inflow ~~type~~conditions, with groups of four bars comparing ~~cases with and without~~ results from WT1 ~~actuation~~operating in greedy and DIC modes, while WT2 remain in greedy mode. Percentage values indicate the relative change ~~in $u_{\mathrm{REWS}}/u_\infty$,~~ with respect to the baseline greedy case. Red arrows alongside bold text highlighting the optimal recovery.

Table 3. ~~Mean thrust coefficient~~ Statistical trends in the mean and standard deviation (~~C_{T}~~ in parentheses) of ~~WT2 with and without~~ $C_{\mathrm{T,WT2}}$ in response to WT1 ~~actuation across~~ operating in greedy or DIC mode under different inflow conditions~~. Standard deviation is shown in parentheses.~~, while WT2 ~~operates~~ remains in greedy mode throughout.

	Uniform inflow				ABL Type-I		ABL Type-II	
St [-]	$A = 1°$		$A = 2°$		$A = 2°$		$A = 2°$	
Greedy	0.17	(~~0.03~~0.04)	0.17	(~~0.03~~0.04)	0.26	(~~0.04~~0.05)	0.36	(~~0.07~~0.08)
0.25	0.22	(~~0.09~~0.11)	0.23	(~~0.12~~0.14)	0.29	(~~0.08~~0.09)	0.37	(~~0.08~~0.09)
0.30	0.23	(~~0.10~~0.12)	0.23	(~~0.12~~0.14)	0.30	(~~0.08~~0.09)	0.38	(~~0.08~~0.09)
0.40	0.23	(~~0.09~~0.12)	0.23	(~~0.11~~0.14)	0.29	(~~0.07~~0.09)	0.37	(~~0.08~~0.09)

fluctuations are less pronounced under ABL inflow conditions, particularly for ABL Type-II, due to the dominant effect of increased ambient turbulence. Moreover, Table 3 summarises ~~the mean C_{T} of WT2 across all investigated cases, with standard deviations shown in parentheses. Due to the improved wake recovery from~~ statistical trends in the mean and standard deviation of $C_{\mathrm{T,WT2}}$. Since WT1 ~~actuation~~pitch actuation improves wake recovery, both the mean ~~C_{T}~~ and standard deviation of ~~WT2~~ $C_{\mathrm{T,WT2}}$ increase across all ~~conditions. However, the effect is less pronounced under ABL inflow, particularly for the ABL Type-II. Under~~ DIC cases compared to the baseline greedy case. The cascading effect on thrust fluctuations is particularly evident in the standard deviation under uniform inflow, ~~the standard deviation increases by up to at~~ with a relative increase of up to 200 % for $A = 1°$ and ~~at~~ 250 % for $A = 2°$. ~~Under~~ Comparatively, under ABL inflow, the ~~fluctuation increase reduces to~~ relative increase is reduced to 80 % for ABL Type-I and 13 % for ABL Type-II.

Furthermore, Fig. 13 compares the power spectra of induced thrust fluctuations ($\phi_{F_{T}'}$) for both WT1 and WT2, zoomed into the St range corresponding to DIC pitch actuation frequencies. Cases under uniform inflow and ABL Type-II are selected to illustrate the cascading behaviour in the spectra for DIC cases with $A = 2°$. Under uniform inflow conditions, the DIC-induced

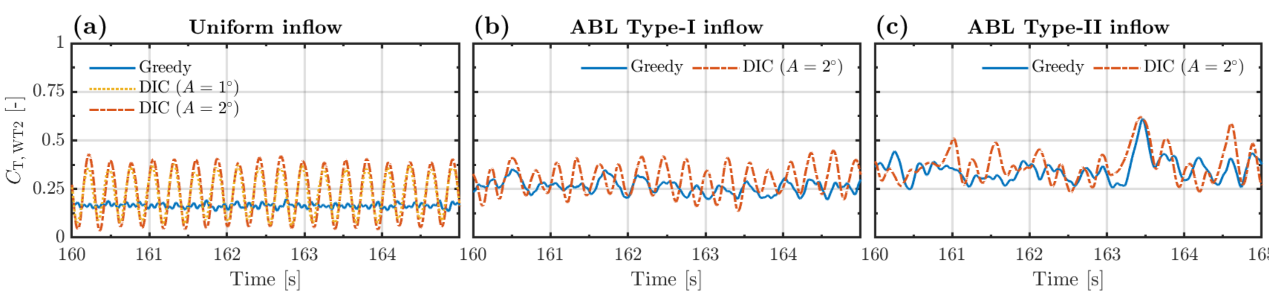

Figure 12. Time series excerpts ~~depicting the impact~~ of ~~WT1 under greedy and DIC operation modes on~~ WT2's thrust coefficient (~~C_{T}~~$C_{\mathrm{T,WT2}}$) ~~across~~ in response to WT1 operating in greedy or DIC mode under different inflow conditions~~.~~, while WT2 remains in greedy ~~operation~~ mode throughout.

peaks not only cascade to WT2 but also exhibit energy levels comparable to those observed at the actuated WT1. This is consistent for both amplitude cases, $A \in \{1°, 2°\}$, explaining why the improvement in WT2's wake recovery is similar or even exceeds that of WT1. Also, note that since WT2 operates within WT1's turbulent wake, its thrust fluctuation energy remains higher even when WT1 operates in greedy mode. In contrast, under ABL inflow conditions, the DIC-induced peaks still cascade to WT2 but with lower energy content compared to WT1, due to the dominant role of ambient turbulence, as noted earlier. This also explains the reduced improvement in WT2's wake recovery improvement under ABL conditions.

3.3 ~~Wind~~ Virtual three-turbine configuration: wind farm power gains

This section evaluates the potential wind farm power gains ~~arising~~ resulting from WT1 ~~actuation with DIC~~ operating in DIC mode relative to the baseline greedy ~~case~~mode. The analysis ~~focuses on a~~ considers a virtual three-turbine ~~array~~ configuration under fully-waked conditions, with ~~a longitudinal spacing~~ longitudinal spacings of 5 D between WT1 and WT2, and 4 D between WT2 and WT3. The first two turbines are physically installed in the tunnel, while ~~the third~~ WT3 is a virtual turbine based on WindScanner data, thereby constituting a real-real-virtual turbine configuration. The 4 D spacing for WT3 ~~was constrained by the WindScanner's~~ is set by the minimum focus distance ~~. The power of~~ of the WindScanner. WT3~~is calculated based on the previously computed~~ 's virtual power is estimated from the u_{REWS} ~~, assuming it operates~~ computed in Sect. 3.2.1, assuming

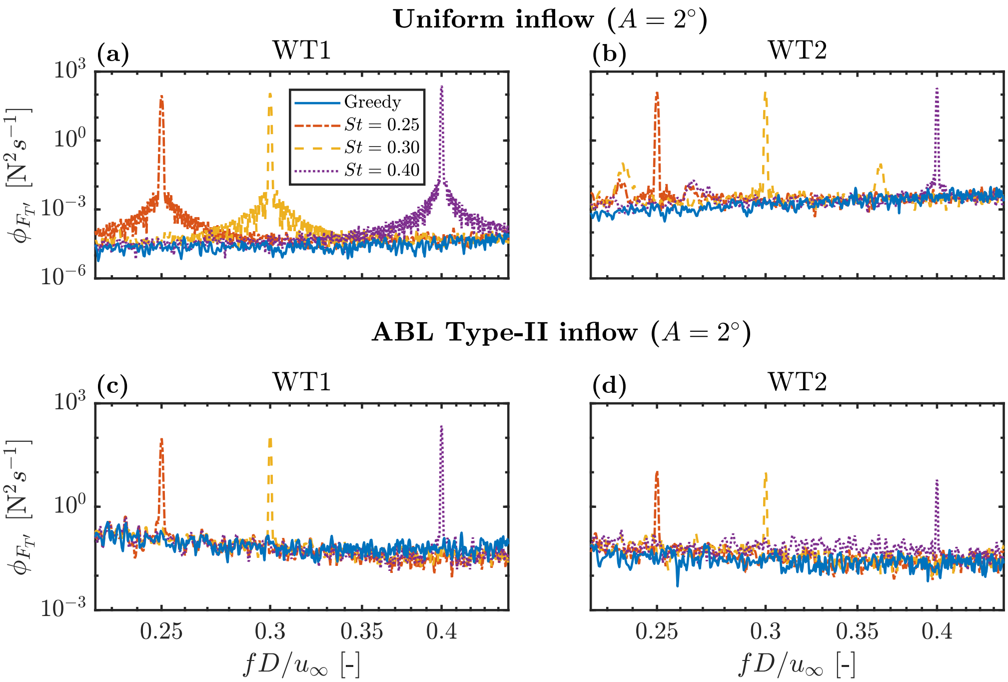

Figure 13. Power spectra of induced thrust fluctuations ($\phi_{F_{T'}}$), zoomed into the St range corresponding to DIC pitch actuation frequencies. Only cases under uniform and ABL type-II inflow conditions are displayed to illustrate the cascading effect in response to WT1 operating in greedy or DIC mode, while WT2 remains in greedy mode throughout.

greedy operation with the same optimal efficiency as WT1 (i.e. $C_{\mathrm{P}} = 0.37$)for all cases, without accounting for Reynolds number effects. Note that Re effects. Accordingly, only WT1 alternates between greedy and DIC modes, while WT2 and WT3 remain in greedy operation throughout. Fig. 12 mode throughout.

Figure 14 displays the mean power ratio (P_i/P_{ref}) for each turbine individual turbines (WT1, WT2, WT3) and for the entire wind farm (WF), based on where P_i represents a 10 min average per case. Each subfigure corresponds to a different inflow type, with P_{ref} representing the of the measured electrical power at WT1 and WT2, and the virtual power of WT3. $P_{\mathrm{ref}} = \sum_{i=1}^{3} P_{i,\mathrm{Greedy}}$ is the total wind farm power output under greedy operation. Percentage values indicate when all three turbines operate in greedy mode. Each subchart corresponds to a different inflow condition, with percentage values indicating the relative change in power due to DIC implementation compared to the greedy case, with bold text highlighting for individual turbines and the whole wind farm with respect to the baseline greedy case. Red arrows alongside bold text highlight the optimal gains due to WT1 actuation.

Experiments In general, experiments under uniform inflow show that the power loss at WT1 increases with amplitude but remains similar across Strouhal numbersoperating in DIC mode experiences higher power losses with increasing pitch amplitude, peaking at 3.4 % for $A = 1°$ and 7.3 % for $A = 2°$. Next, while losses remain similar across all St cases. For WT2,

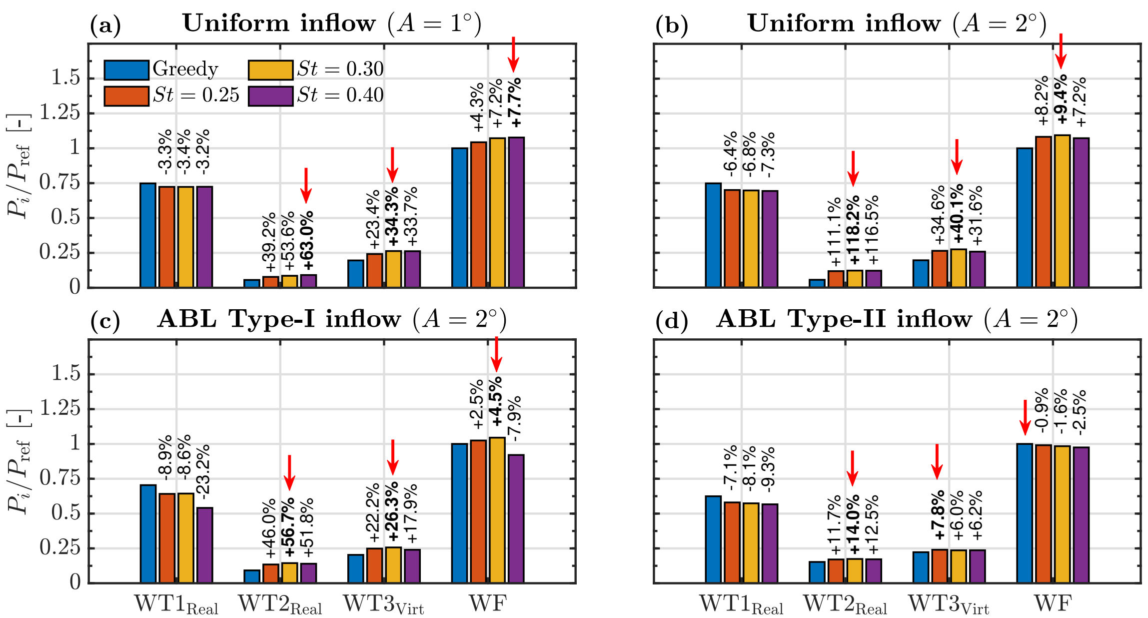

Figure 14. Wind farm power gain using a real-real-virtual turbine configuration. The power ratio (P_i/P_{ref}) is shown for individual turbines (WT1, WT2, WT3) and the overall wind farm (WF), with WT1 operating in both greedy and DIC modes, while WT2 and virtual WT3 remain in greedy mode. Each subchart corresponds to a different inflow condition. Percentage values indicate the relative change with respect to the baseline greedy case, with P_{ref} representing the wind farm power with all turbines in greedy mode. Red arrows alongside bold text highlight the optimal gains.

the highest power gains at WT2 occur at $St = 0.40$ for $A = 1°$ and $St = 0.30$ for $A = 2°$, with the optimal gain nearly doubling when moving from the lower to the higher amplitude . Specifically, it reaches optimal gains nearly doubling as amplitude increases, reaching 63.0 % at $A = 1°$ and 118.2 % at $A = 2°$. The same behaviour is observed in terms of These trends align with the wake recovery improvement shown in Fig. 6. Furthermore, the power gain at However, it is worth noting that the relative gains based on WT2's power measurements are higher than those estimated from virtual power using WindScanner data (cf. Appendix C1, where WT2's virtual power is computed in the same manner as for virtual WT3is highest at). This discrepancy arises from the C_P dependence on Re, which reduces aerodynamic efficiency at lower wind speeds. Consequently, the power gain at WT2 reflects both the effective increase in wind speed due to DIC, as well as the increase in C_P. The latter is a drawback of wind tunnel testing, resulting in smaller wind farm power gains but without affecting the qualitative trends, as described in Appendix C. In contrast, power estimates at virtual WT3 inherently compensate for the C_P dependence on Re, as the virtual power is computed assuming a constant C_P across all cases. This assumption more closely resembles the behaviour of full-scale turbines but leads to higher power estimates for virtual WT3 compared to WT2 measurements. Nevertheless, the overall trends remain consistent regardless of the assumed C_P. Specifically, the power gain at WT3 peaks at $St = 0.30$ for both amplitudesamplitude cases, with slightly higher gains at $A = 2°$higher amplitude, reaching 34.3 % at $A = 1°$ and 40.1 % at $A = 2°$. Overall, the combined wind farm power gain reaches up to 7.7 % and 9.4 % for the $A = 1°$ and $A = 2°$ cases, respectively.

Power ratio (P_i/P_ref) of individual turbines (WT1, WT2, WT3) and wind farm (WF) for both greedy and DIC cases, with P_ref representing the total wind farm power output under greedy operation. Each subchart corresponds to a different inflow type. Percentage values indicate the relative change in P_i/P_ref due to DIC compared to the greedy case. Bold text highlights the optimal gains. For the experiments under Under ABL inflow, the power loss at WT1 remains similar is generally comparable to that observed in uniform inflow casesunder uniform inflow conditions, except for the DIC case with $St = 0.40$ under ABL Type-I, which exhibits a significantly substantially higher loss of 23.2 %. This may be attributed to unfavorable interactions (e.g., vibrations or resonances) between the turbine actuation at this particular setting and the turbulence characteristics of ABL Type-I. For this inflow, the power gains at Power spectrum analysis of the torque signal revealed a significant increase in low-frequency energy content compared to other DIC cases, indicating that the loss was driven by large fluctuations in generator torque, which in turn caused significant power fluctuations. This is suspected to have been caused by a bug in the turbine's operating code introducing communication delays in the system after long run-time. Nevertheless, consistent with trends in wake recovery improvement (Sect. 3.1.1 and 3.2.1), the relative power gain for WT2, virtual WT3, and WF align the wind farm aligns with $St = 0.30$, reaching up to for ABL type-I, peaking at 56.7 %, 26.3 %, and 4.5 %respectively. For the , respectively. Also in agreement with wake recovery trends, the relative power gain is reduced for ABL Type-IIinflow, , peaking at 14.0 % with $St = 0.30$ for WT2 and WT3 achieve smaller power gains of up to and 7.8 % , respectively, with $St = 0.25$ for WT3, with no net gain at the farm level.

4 Discussion

This study ~~investigated~~ provides insights into the wake recovery improvement induced by DIC as a function of pitch amplitude and Strouhal number, along with its cascading effects on a downstream turbine operating in greedy mode and the resulting wind farm power gains under baseline uniform inflow and two realistic ABL inflows. To this end, wind tunnel experiments were conducted ~~using~~ in single- and two-turbine configurations~~to map the wake response of each turbine under baseline uniform inflow and two realisitic ABL conditions~~, incorporating an active grid to generate atmospheric-like inflows, WindScanner lidar measurements to remotely map the wakes of individual turbines and an array of hot wires to analyse the wake turbulence development.

Compared to conventional wind tunnel techniques such as particle image velocimetry (PIV) and laser Doppler anemometry (LDA), WindScanner measurements ~~enabled~~ enable flexible and efficient remote mapping of ~~each turbine's wake~~ turbine wakes at multiple downstream locations with high spatial resolution. Depending on the experimental setup and WindScanner operation mode (staring or scanning), phase-averaged characteristics, turbulence dissipation rates, spectral or time series data can be analysed, albeit constrained by the maximum temporal resolution of 451.7 Hz and the probe-volume averaging effect (Hulsman et al., 2022b; van Dooren et al., 2022). ~~While this studyfocused on~~ In this study, WindScanner measurements were used to obtain highly spatially resolved time-averaged wake characteristics ~~,~~ at different downstream locations, while complementary hot-wire measurements ~~provided indication on the level of DIC-added local turbulence~~ gave insights into the local turbulence development in the wake of a DIC-actuated turbine.

~~In general, the experimental results~~ First, results from the single-turbine configuration show that DIC ~~enhances the wake recovery of both the actuated~~ actuation consistently enhances WT1~~and the greedy WT2 across all cases compared to the baseline greedy case. This effect is particularly pronounced at higher pitch amplitudes ($A = 2°$), while variations across different Strouhal numbers remain minor. This finding suggests a stronger control authority achieved through~~'s wake recovery across all tested combinations of pitch amplitude and Strouhal number. However, the level of DIC-added recovery responds more positively to increased forcing amplitude than ~~with a higher Strouhal number~~to changes in St. This behaviour is attributed to ~~higher amplitudes of C_T oscillations , which enhance turbulent mixing by introducing higher levels of DIC-added local turbulence, as evidenced in~~ the magnitude of induced thrust oscillations ($C_{T,WT1}$) and turbulence development in the wake. As shown in Fig. 7, increasing St at constant amplitude yields minor variations in local TI, whereas increasing amplitude at fixed St produces a marked rise in local TI, further accelerating the onset of wake recovery. More intricately, the optimal St depends not only on the level of induced thrust fluctuations (Sect. ~~??.Consistent~~ 3.1.3) but also on the spatial development of coherent structures (Fig. 8), which is in turn influenced by both the forcing amplitude and inflow turbulence. Furthermore, consistent with numerical studies (Munters and Meyers, 2018; Yılmaz and Meyers, 2018), the wake recovery ~~improvement induced~~ enhancement achieved by DIC decreases under ~~turbulent and sheared~~ strongly sheared and highly turbulent inflow conditions. This effect ~~is exacerbated by increasing inflow~~ relates to the dominant role of high ambient turbulence, which inherently ~~enhances~~ promotes natural wake mixing~~and results in higher standard deviations of C_T, even without turbine actuation. This is expected to reduce~~, thereby reducing the control authority ~~of DIC, particularly under unstable atmospheric conditions, and~~

should be explored in future studiesachieved through DIC-induced $C_{\mathrm{T,WT1}}$ fluctuations. Nonetheless, this study demonstrated improved wake recovery even under highly sheared and turbulent inflow, highlighting DIC's potential adaptability underscores the potential adaptability of DIC to realistic inflow conditions.

A novel contribution of this research is the evaluation of the cascading effects Second, results from the two-turbine configuration shed light on the cascading effect of WT1 actuation on the wake recovery of a downstream turbine , operating (WT2). Remarkably, despite remaining in greedy mode. Notably, WT2exhibits periodic oscillations of C_{T} in response to WT1 actuation, which are assumed to be the triggering factor for the improved WT2's wake recovery . This effect may be attributed to wake synchronisation with the harmonic forcing of DIC is consistently enhanced when WT1 operates in DIC mode. This enhancement is attributed to the dynamic coupling between WT1's wake and the periodic DIC perturbation at WT1, which causes 's rotor plane, which induces a pulsating flow pattern at the pitch actuation frequency (Fig. 8). Consequently, WT2 to experience higher average wind speeds accompanied by periodic fluctuations (Yılmaz and Meyers, 2018).Consequently, both the mean C_{T} and standard deviation of exhibits periodic $C_{\mathrm{T,WT2}}$ fluctuations with energy levels comparable to those at the DIC-actuated WT1 (Fig. 13), which are assumed to drive the enhanced recovery. As a result, WT2increase relative to the baseline greedy case.Similar to single-turbine experiments, the cascading effects decrease with increased inflow turbulence. Future work should aim to better understand and evaluate the cascading effects of DIC.

Unlike experiments under uniform and ABL Type-I inflow, the wake re-energisation induced by DIC at 's wake recovery is similar to, or even exceeds, that of WT1 exhibits an asymmetric behaviour under ABL Type-II inflow (Fig. 5j-l). This can be partially attributed to the influence of wake rotation under sheared inflow, where high-speed momentum is transported downward and low-speed momentum upward. Consequently, 11). Interestingly, WT2's optimal recovery predominantly aligns with WT1 actuation at St = 0.30 across all inflow conditions. Moreover, as in the single-turbine experiments, the wake of a non-misaligned, greedy turbine tends to be slightly deflected to the right when viewed from downstream (Fleming et al., 2014; Gebraad et a . This effect is particularly enhanced under highly sheared and turbulent inflow but appears to be disturbed by DIC. Furthermore, DIC enhances the mechanical turbulenceinduced by the nacelle and tower (van der Hoek et al., 2022). Since TI levels below hub height are typically reduced relative to undisturbed ABL inflow (Porté-Agel et al., 2020), this additional TI may explain the increase in available wind speed, initially concentrated below hub height and gradually spreading over the rotor area further downstream. Future studies cascading effects decrease with increasing inflow turbulence. Future work should further explore the complex turbulent interactions between DIC-actuated turbines and ABL inflows. these cascading effects, particularly from a fundamental fluid dynamics perspective.

Another important aspect to highlight is that, compared to previous studies based on numerical simulations with full-scale turbines (e.g. Yılmaz and Meyers, 2018; Frederik et al., 2020a; Coquelet et al., 2022), the power losses due to DIC in Third, the assessment of wind farm power gains in a virtual three-turbine configuration demonstrates consistent power benefits under uniform and ABL Type-I inflows. The absence of net power gains at the farm level under ABL Type-II is primarily due to the higher power losses experienced by the model wind turbine are more pronounced (approximately 10 %) , especially when higher amplitude is combined with a higher Strouhal number. This issue has also been observed in previous wind tunnel studies (e.g. Frederik et al., 2020b; van der Hoek et al., 2022, 2024), which attribute it to a steeper power curve, typical of

~~model turbines, or to potential vibrations caused by slight rotor imbalances. Nevertheless, it is anticipated that such losses would be smaller~~ compared to those expected in full-scale ~~applications~~turbines. Supporting this, ~~the aerolastic simulations presented in Appendix ??,~~ aerolastic simulations using the NREL–5 MW reference turbine ($D = 126\,\mathrm{m}$) ~~, indicate~~ show power losses below 1.6 % for all DIC cases under both uniform and ABL ~~inflow conditions. Despite the model turbine experiencing higher power losses, the study demonstrated wind farm power gains under both uniform inflow and ABL Type-I inflow, the latter exhibiting characteristics resembling atmospheric stable conditions. This underscores the potential~~ inflows (cf. Appendix D). These results are more closely aligned with reported losses from LES studies using actuator disc or actuator line models (e.g. Yılmaz and Meyers, 2018; Frederik et al., 2020a; Coquelet et al., 2022). Moreover, the increased power losses are a limitation of the model wind turbine, whose power curve is more sensitive to pitch angle variations, likely due to reduced airfoil efficiency in low-Re regimes. Consequently, higher average power losses occur when DIC mode is active. Such behaviour has been observed in previous wind tunnel studies with comparable model turbines (e.g. Frederik et al., 2020b; van der Hoek et a . Nevertheless, the findings highlight the potential wind farm power benefits of DIC implementation in realistic inflow ~~scenarios, particularly for low TI conditions~~conditions, particularly in low-turbulence environments, which typically ~~results in~~ exhibit more persistent wakes.

~~Interestingly,~~ Furthermore, it is worth noting that the optimal wind farm power gains are predominantly achieved with WT1 actuation at $St = 0.30$ and $A = 2°$. This ~~finding closely aligns~~ aligns closely with the optimal Strouhal number identified in previous wind tunnel studies ~~with three-turbines (Frederik et al., 2020b; Wang et al., 2020). While the optimal gain at~~ using a three-turbine configuration (Frederik et al., 2020b; Wang et al., 2020). Although the optimal gains with low amplitude ($A = 1°$~~was achieved with~~) are achieved at $St = 0.40$, the net power gains ~~were~~ remain similar to those obtained with $St = 0.30$. This suggests that adopting a single Strouhal number could simplify integration into a real wind farm controller while providing comparable benefits. ~~Furthermore, the impact of increasing pitch amplitude proved to be more significant, with greater variations in the achievable gains. Although~~ In line with wake recovery trends, a greater impact on power gains is observed with increased pitch amplitude rather than increased St. While this study was limited to two amplitude cases, it can be inferred that the maximum DIC amplitude should be constrained to limit structural loads, as ~~suggested~~ recommended for the helix approach (Taschner et al., 2023). ~~In addition, for the adopted setting with full wake overlap and turbine spacings of 5 D and 4 D, the results indicate that the largest increase in power occurs at WT2, although considerable gains are also observed at the virtual turbine WT3. Note that the level of power gain at the virtual turbine WT3 is likely underestimated, as the Reynolds number dependency of the turbine's power coefficient was not considered in the analysis.~~

~~Future studies should focus on fatigue load analysis to identify the trade-off~~ Accordingly, future studies should explore the trade-offs between power benefits and structural load penalties. ~~Frederik and van Wingerden (2022) provide one of the most comprehensive studies examining the impact of wake mixing strategies on different turbine components. Based on FAST and SOWFA simulations, the study shows~~ For instance, Frederik and van Wingerden (2022) reports that DIC primarily affects the tower fore-aft bending moment, ~~with no observed risk of pitch bearing damage~~ without introducing additional risk to the pitch bearing compared to conventional individual pitch control (IPC) for load alleviation. ~~Furthermore, a first step before field validation could involve wind tunnel testing~~ To further investigate load impacts, wind tunnel experiments with aeroelastic model wind turbines capable of ~~providing~~ meaningful load analysis ~~. Another relevant aspect would be testing~~ would be valuable. Additionally, assessing the robustness of ~~the~~ optimal control parameters under dynamic inflow conditions, ~~with~~ such as varying wind direction, turbulence intensity, and wind speeds, remains a key aspect for future research.

5 Conclusions

This study investigated the potential of DIC to improve wake recovery in single- and two-turbine configurations, as well as potential wind farm power gains in a virtual three-turbine ~~array incorporating a virtual turbine~~configuration. This encompassed experiments under baseline uniform inflow and two realistic ABL inflow conditions. WindScanner measurements ~~facilitated the examination~~ enabled detailed analysis of WT1's wake recovery at different pitch amplitudes $A \in \{1°, 2°\}$ and Strouhal numbers $St \in \{0.25, 0.30, 0.40\}$, ~~as well as~~ along with its cascading effects on the wake of a downstream turbine WT2, operating in greedy mode. Compared to ~~baseline greedy operation~~the baseline greedy mode, the results ~~show~~ showed improved wake recovery of both WT1 and WT2 ~~through sole actuation of~~ solely through WT1 ~~. This trend persists~~ actuation. This improvement persisted across all DIC cases and inflow scenarios, yet the degree of DIC-added recovery ~~decreases~~ decreased with increasing inflow turbulence. The study also ~~provides~~ provided insights into the ~~relationship~~ interplay between optimal excitation frequency and pitch amplitude. Notably, stronger control authority ~~is achieved with higher~~ was achieved by increasing pitch amplitude rather than ~~higher~~ Strouhal number, as ~~increased amplitude enhances turbulent mixing through more pronounced periodic thrust fluctuations~~higher amplitudes produced a faster turbulence build-up and transition to the far-wake region. Within the considered range, optimal gains ~~are~~ were observed at higher Strouhal numbers for lower pitch amplitudes, and vice versa. This ~~is~~ was evidenced by both WindScanner wake measurements and WT2's power output. Furthermore, the study ~~demonstrates~~ demonstrated wind farm power gains not only under uniform inflow but also under turbulent and sheared inflow. Overall, ~~this study contributes to validate~~ these findings support DIC's potential as an promising wind farm flow control strategy, demonstrating consistent benefits and adaptability under realistic inflow conditions.

Future research should include fatigue load analyses to balance power gains with structural load penalties, as increased pitch parameters, either independently or together, ~~can~~ may exacerbate fatigue loading and power losses ~~in~~ at the actuated turbine. Further exploration of DIC under dynamic inflow conditions could also extend its applicability or potential integration with more advanced strategies, such as wake steering control.

Data availability. The experimental datasets are available at https://doi.org/10.5281/zenodo.15356141 (Zúñiga Inestroza et al., 2025)

Appendix A: WindScanner measurement uncertainty

To illustrate the uncertainty in wake measurements obtained with the lidar WindScanner, Fig. A1a-c presents contours of the relative error (e_u/u) introduced by the single-Doppler reconstruction of u at downstream distances $x/D \in \{2, 5, 9\}$,

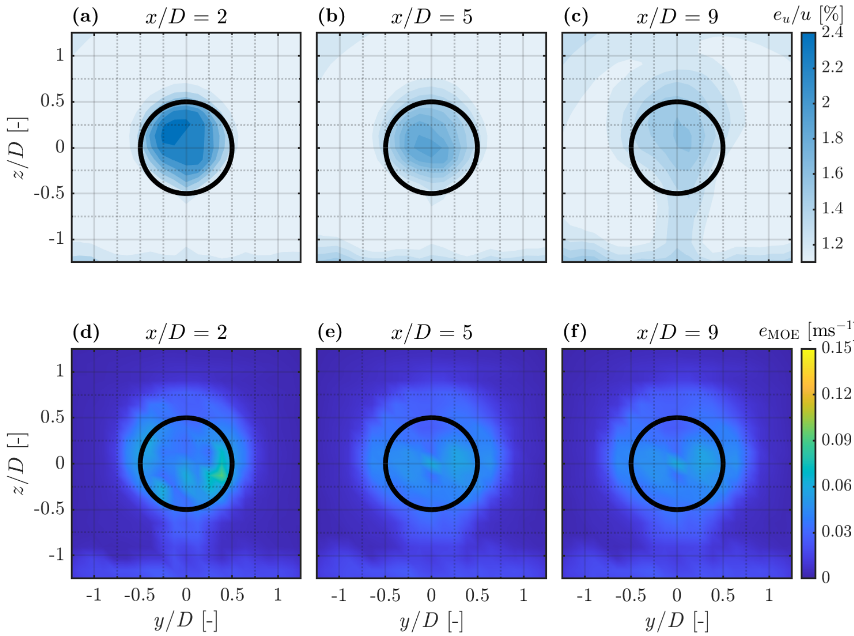

Figure A1. Uncertainty in the streamwise velocity component measured with the WindScanner at downstream distances $x/D \in \{2,5,9\}$. The top row (a-c) shows the relative error (e_u/u) introduced by the single-Doppler reconstruction, while the bottom row (d-f) presents the statistical margin of error (e_{MOE}). All wake contours correspond experiments under uniform inflow with upstream turbine actuation at $St = 0.30$ and $A = 2°$.

while Fig. A1d-f shows the corresponding statistical uncertainty at the same locations. The displayed contours correspond to experiments under uniform inflow with WT1 actuation at $St = 0.30$ and $A = 2°$. The analysis of e_u/u follows the standard uncertainty propagation method (JCGM, 2008; van Dooren et al., 2017; Hulsman et al., 2022b), expressed as:

$$e_u = \sqrt{\left(\frac{\partial u}{\partial v_{\mathrm{los}}}\delta_{v_{\mathrm{los}}}\right)^2 + \left(\frac{\partial u}{\partial v}\delta_v\right)^2 + \left(\frac{\partial u}{\partial w}\delta_w\right)^2 + \left(\frac{\partial u}{\partial \phi}\delta_\phi\right)^2 + \left(\frac{\partial u}{\partial \theta}\delta_\theta\right)^2}, \tag{A1}$$

where $\delta_{v_{\mathrm{los}}}$ is the uncertainty of the measured line-of-sight wind speed, assumed to be 1 % of u_∞. δ_v and δ_w represent the uncertainties arising from neglecting the v and w components, conservatively assumed as 1 ms^{-1}. δ_ϕ and δ_θ refer to the uncertainties in the azimuth and elevation angles, each assumed to be 0.5 mrad. Additionally, the statistical uncertainty is expressed in terms of the margin of error $e_{\mathrm{MOE}} = z_\gamma \sigma/\sqrt{N}$, where $z_\gamma = 1.96$ is the quantile corresponding to a 95 % confidence interval, σ is the standard deviation of the measurements and N is the sample size.

In general, e_u/u is higher within the wake and closer to the rotor, since the wind speed deficit is more pronounced. Similarly, a higher e_{MOE} is observed in regions of higher turbulence due to increased fluctuations within the wake.

Appendix B: Wind speed deficit profiles

To illustrate the differences among DIC cases with increasing Strouhal number, ~~$St \in \{0.25, 0.30, 0.40\}$~~$St \in \{0.25, 0.30, 0.40\}$, Fig. ~~A1~~ B1 presents horizontal wake profiles of WT1. Each row depicts the wind speed deficit at hub height $(1 - u/u_\infty)$ across different inflow conditions at downstream locations ~~$x/D \in \{2, 4, 5\}$~~$x/D \in \{2, 4, 5\}$. Similarly, Fig. ~~??~~ B2 displays wind speed deficit profiles of WT2, comparing cases with and without WT1 actuation at downstream locations $x'/D \in \{2, 4\}$.

Appendix C: Validation of wind farm power gain trends

To validate the qualitative trends observed in Fig. 14, a virtual three-turbine configuration is considered, where only WT1 is based on power measurements, while WT2 and WT3 are virtual turbines whose power is estimated from u_{REWS} following the method outlined in Sect. 3.3. This approach eliminates the influence of Re on aerodynamic efficiency (C_{P}) of the model turbine, isolating the effect of DIC on wake recovery and downstream performance. Fig. C1 presents the corresponding mean power ratio (P_i/P_{ref}) for individual turbines and the overall wind farm. While the relative magnitude of power gains changes slightly compared to the real–real–virtual configuration used in the main analysis, the qualitative trends remain consistent.

Appendix D: Power detriment in a full-scale actuated turbine

To address the ~~higher~~ high power losses experienced by the model wind turbine due to DIC activation, aeroelastic simulations ~~were~~ are performed in OpenFAST v3.4.1 (Jonkman et al., 2023) using the full-scale NREL–5 MW reference turbine ($D = 126\,\mathrm{m}$). ~~All simulations were~~ To account for unsteady aerodynamic effects, the Beddoes-Leishman unsteady aerodynamic model is employed. All simulations are conducted at $u_\infty = 7.0\,\mathrm{m\,s^{-1}}$ to match the wind tunnel conditions. TurbSIM (Jonkman, 2009) ~~was~~ is used to generate ABL inflows with the same power-law exponent and turbulence intensity values described in Sect. 2.5. Table ~~??~~ D1 summarises the $10\,\mathrm{min}$ averaged power losses experienced by the actuated turbine relative to the baseline greedy case. ~~Overall~~In general, DIC cases at $A = 2°$ exhibit power losses below $1.6\,\%$ across all inflow conditions, decreasing to around $0.4\,\%$ at $A = 1°$. Therefore, despite some simplifications inherent OpenFAST simulations, the results provide reasonable indication that power losses in full-scale turbines are likely smaller than those experienced by the model turbine.

Author contributions. MAZI designed and conducted the wind tunnel measurement campaign, performed the data analysis and wrote the manuscript. PH assisted during the measurement campaign and data analysis. VP contributed to design the measurement campaign, data analysis and structuring the manuscript. MK supervised the research. All co-authors contributed through discussions and thoroughly reviewed the manuscript.

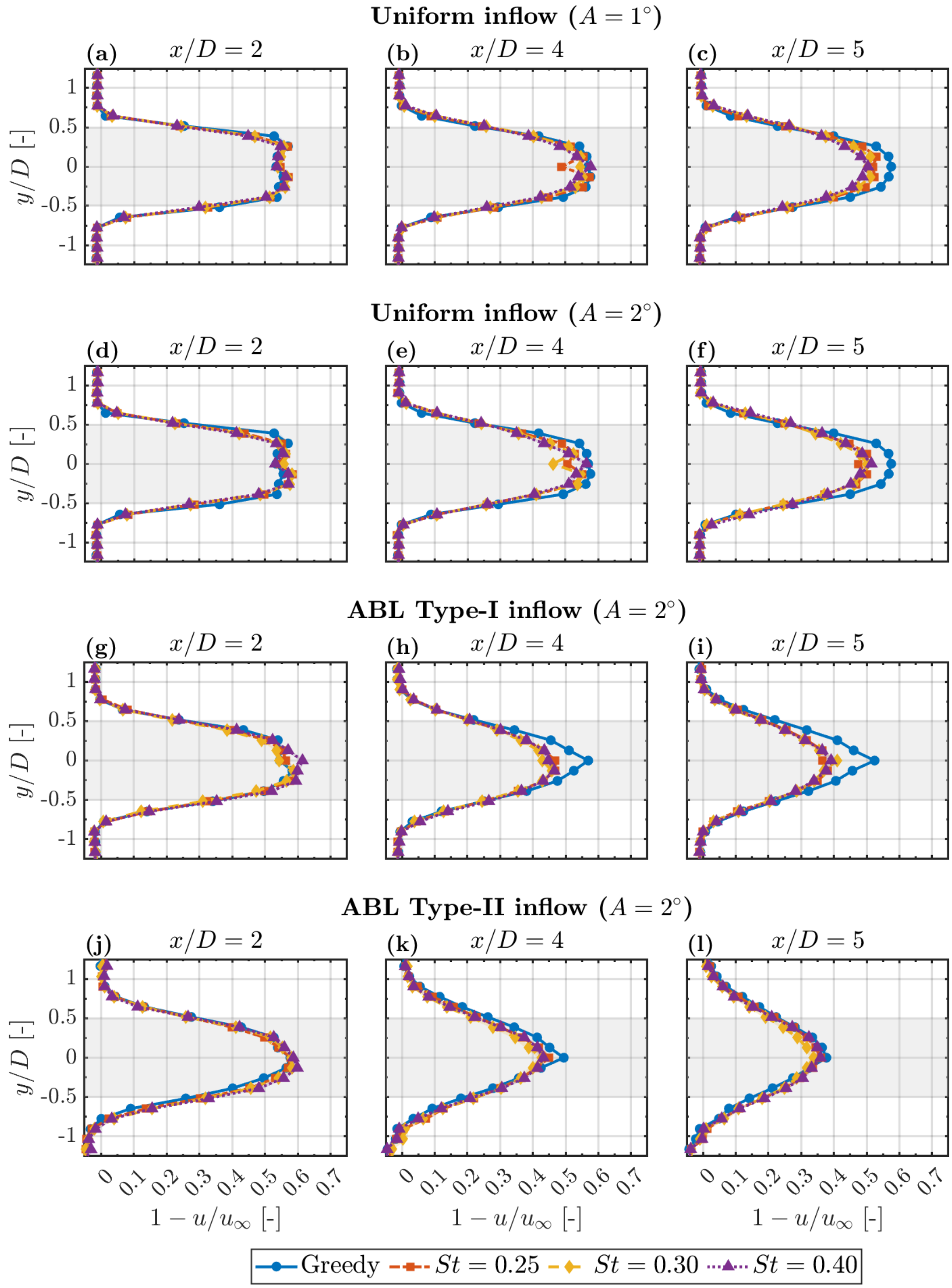

Figure B1. Horizontal wake profiles of WT1 showing the wind speed deficit at hub height ($1 - u/u_\infty$) under greedy and DIC cases. Each row corresponds to a different inflow type at downstream distances $x/D \in \{2, 4, 5\}$. Shaded grey regions indicate the rotor swept area.

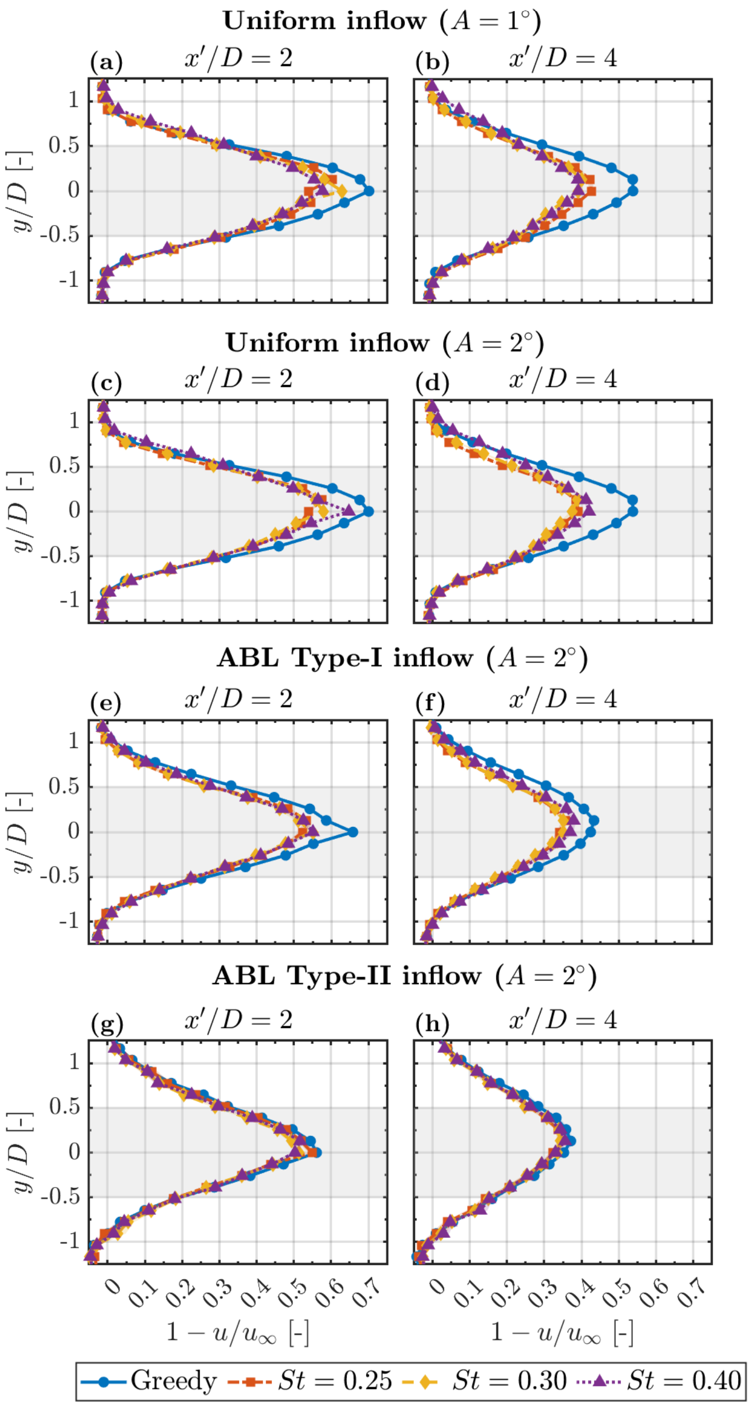

Figure B2. Horizontal wake profiles of WT2 showing the wind speed deficit at hub height ($1 - u/u_\infty$). In all cases, WT2 remains in greedy operation, while WT1 alternates between greedy and DIC modes. Each row corresponds to a different inflow type at downstream distances $x'/D \in \{2, 4\}$. Shaded grey regions indicate the rotor swept area.

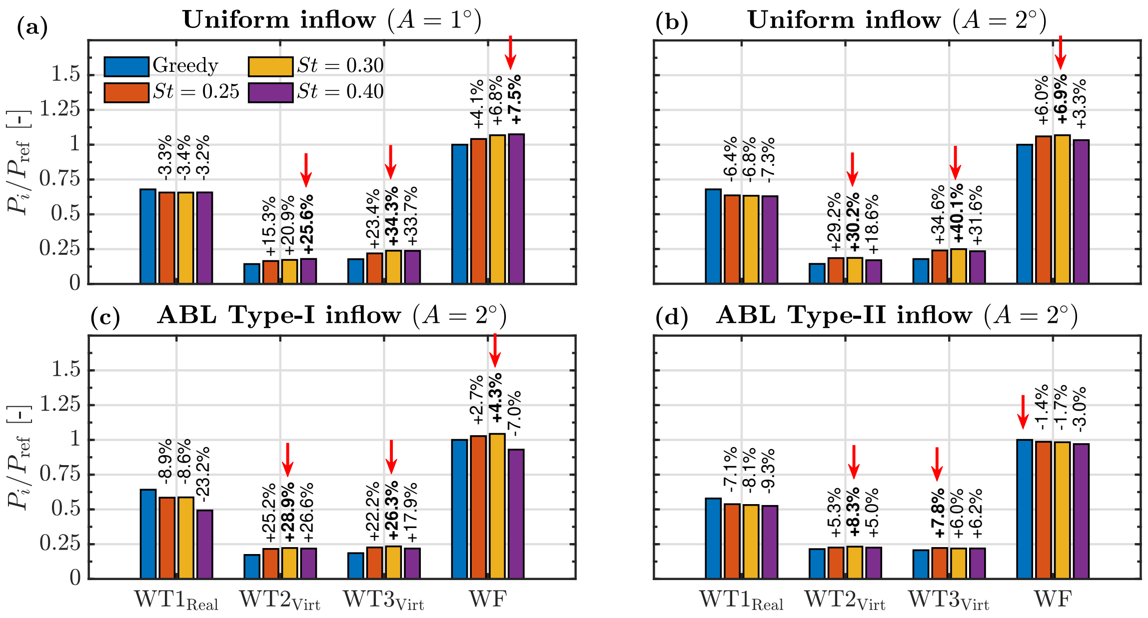

Figure C1. Validation of wind farm power gain trends using a real–virtual–virtual turbine configuration. The power ratio (P_i/P_{ref}) is shown for individual turbines (WT1, WT2, WT3) and wind farm (WF), with WT1 operating in both greedy and DIC modes, while virtual WT2 and virtual WT3 remain in greedy mode. Each subchart corresponds to a different inflow condition. Percentage values indicate the relative change with respect to the baseline greedy case, with P_{ref} representing the wind farm power with all turbines in greedy mode. Red arrows alongside bold text highlight the optimal gains.

Table D1. Power loss at WT1 due to DIC relative to the greedy case, shown as a function of pitch amplitude and Strouhal number across different inflow conditions. Results are based on OpenFAST simulations using the NREL–5 MW reference turbine ($D = 126$ m).

	Uniform inflow		ABL Type-I	ABL Type-II
St [-]	$A = 1°$	$A = 2°$	$A = 2°$	$A = 2°$
0.25	-0.37	-1.49	-1.47	-1.34
0.30	-0.39	-1.51	-1.49	-1.37
0.40	-0.41	-1.55	-1.53	-1.39

Competing interests. The authors declare that they have no conflict of interest.

Acknowledgements. This research is partly funded by the German Academic Exchange Service (DAAD) and by the Federal Ministry for Economic Affairs and Energy according to a resolution by the German Federal Parliament in the scope of research project DFWind (Ref. Nr.

0325936C). We thankfully acknowledge Anantha Padmanabhan Kidambi Sekar, Apostolos Langidis, David Onnen, Juan Manuel Boullosa Novo, Julian Jüchter, Lars Neuhaus, Marijn Floris van Dooren and Raghawendra Joshi for their assistance during the measurement campaign.

References

Barthelmie, R. J. and Jensen, L. E.: Evaluation of wind farm efficiency and wind turbine wakes at the Nysted offshore wind farm, Wind Energy, 13, 573–586, https://doi.org/https://doi.org/10.1002/we.408, 2010.

Boersma, S., Doekemeijer, B., Gebraad, P., Fleming, P., Annoni, J., Scholbrock, A., Frederik, J., and van Wingerden, J.-W.: A tutorial on control-oriented modeling and control of wind farms, in: 2017 American Control Conference (ACC), pp. 1–18, https://doi.org/10.23919/ACC.2017.7962923, 2017.

Bossanyi, E. A.: The Design of closed loop controllers for wind turbines, Wind Energy, 3, 149–163, https://doi.org//10.1002/we.34, 2000.

Brown, K., Yalla, G., Cheung, L., Frederik, J., Houck, D., deVelder, N., Simley, E., and Fleming, P.: Comparison of wind-farm control strategies under realistic offshore wind conditions: wake quantities of interest, Wind Energy Science Discussions, 2025, 1–39, https://doi.org/10.5194/wes-2024-191, 2025.

Cal, R. B., Lebrón, J., Castillo, L., Kang, H. S., and Meneveau, C.: Experimental study of the horizontally averaged flow structure in a model wind-turbine array boundary layer, Journal of Renewable and Sustainable Energy, 2, 013 106, https://doi.org/10.1063/1.3289735, 2010.

Chamorro, L. P., Arndt, R., and Sotiropoulos, F.: Reynolds number dependence of turbulence statistics in the wake of wind turbines, Wind Energy, 15, 733–742, https://doi.org/https://doi.org/10.1002/we.501, 2012.

Coquelet, M., Moens, M., Bricteux, L., Crismer, J.-B., and Chatelain, P.: Performance assessment of wake mitigation strategies, J. Phys. Conf. Ser., 2265, 032 078, https://doi.org/10.1088/1742-6596/2265/3/032078, 2022.

Dallas, S., Stock, A., and Hart, E.: Control-oriented modelling of wind direction variability, Wind Energy Science, 9, 841–867, https://doi.org/10.5194/wes-9-841-2024, 2024.

Fleming, P., Gebraad, P. M., Lee, S., van Wingerden, J.-W., Johnson, K., Churchfield, M., Michalakes, J., Spalart, P., and Moriarty, P.: Simulation comparison of wake mitigation control strategies for a two-turbine case, Wind Energy, 18, 2135–2143, https://doi.org//10.1002/we.1810, 2015.

Fleming, P. A., Gebraad, P. M., Lee, S., van Wingerden, J.-W., Johnson, K., Churchfield, M., Michalakes, J., Spalart, P., and Moriarty, P.: Evaluating techniques for redirecting turbine wakes using SOWFA, Renewable Energy, 70, 211–218, https://doi.org//10.1016/j.renene.2014.02.015, 2014.

Frederik, J. A. and van Wingerden, J.-W.: On the load impact of dynamic wind farm wake mixing strategies, Renewable Energy, 194, 582–595, https://doi.org//10.1016/j.renene.2022.05.110, 2022.

Frederik, J. A., Doekemeijer, B. M., Mulders, S. P., and van Wingerden, J.-W.: The helix approach: Using dynamic individual pitch control to enhance wake mixing in wind farms, Wind Energy, 23, 1739–1751, https://doi.org//10.1002/we.2513, 2020a.

Frederik, J. A., Weber, R., Cacciola, S., Campagnolo, F., Croce, A., Bottasso, C., and van Wingerden, J.-W.: Periodic dynamic induction control of wind farms: proving the potential in simulations and wind tunnel experiments, Wind Energy Sci., 5, 245–257, https://doi.org/10.5194/wes-5-245-2020, 2020b.

Gebraad, P. M. O., Teeuwisse, F. W., van Wingerden, J. W., Fleming, P. A., Ruben, S. D., Marden, J. R., and Pao, L. Y.: Wind plant power optimization through yaw control using a parametric model for wake effects—a CFD simulation study, Wind Energy, 19, 95–114, https://doi.org/https://doi.org/10.1002/we.1822, 2016.

Goit, J. P. and Meyers, J.: Optimal control of energy extraction in wind-farm boundary layers, J. Fluid Mech., 768, 5–50, https://doi.org/10.1017/jfm.2015.70, 2015.

Goit, J. P., Munters, W., and Meyers, J.: Optimal Coordinated Control of Power Extraction in LES of a Wind Farm with Entrance Effects, Energies, 9, https://doi.org/10.3390/en9010029, 2016.

Houck, D. R.: Review of wake management techniques for wind turbines, Wind Energy, 25, 195–220, https://doi.org//10.1002/we.2668, 2022.

Howland, M. F., González, C. M., Martínez, J. J. P., Quesada, J. B., Larrañaga, F. P., Yadav, N. K., Chawla, J. S., and Dabiri, J. O.: Influence of atmospheric conditions on the power production of utility-scale wind turbines in yaw misalignment, Journal of Renewable and Sustainable Energy, 12, 063 307, https://doi.org/10.1063/5.0023746, 2020.

Hulsman, P., Wosnik, M., Petrović, V., Hölling, M., and Kühn, M.: Turbine Wake Deflection Measurement in a Wind Tunnel with a Lidar WindScanner, Journal of Physics: Conference Series, 1452, 012 007, https://doi.org/10.1088/1742-6596/1452/1/012007, 2020.

Hulsman, P., Sucameli, C., Petrović, V., Rott, A., Gerds, A., and Kühn, M.: Turbine power loss during yaw-misaligned free field tests at different atmospheric conditions, Journal of Physics: Conference Series, 2265, 032 074, https://doi.org/10.1088/1742-6596/2265/3/032074, 2022a.

Hulsman, P., Wosnik, M., Petrović, V., Hölling, M., and Kühn, M.: Development of a curled wake of a yawed wind turbine under turbulent and sheared inflow, Wind Energy Sci., 7, 237–257, https://doi.org/10.5194/wes-7-237-2022, 2022b.

Hulsman, P., Howland, M., Göçmen, T., Petrović, V., and Kühn, M.: Self-Learning Data-Driven Wind Farm Control Strategy Using Field Measurements, pp. 1057–1064, https://doi.org/10.23919/ACC60939.2024.10644839, 2024.

JCGM: Evaluation of measurement data: Guide to the expression of uncertainty in measurement, https://doi.org/10.59161/JCGM100-2008E, 2008.

Jonkman, B., Mudafort, R. M., Platt, A., Branlard, E., Sprague, M., jjonkman, Ross, H., HaymanConsulting, Hall, M., Vijayakumar, G., Buhl, M., Bortolotti, P., Ananthan, S., S., M., Rood, J., rdamiani, nrmendoza, sinolonghai, pschuenemann, Slaughter, D., ashesh2512, kshaler, Housner, S., psakievich, Bendl, K., Carmo, L., Quon, E., mattrphillips, Kusuno, N., and Salcedo, A. G.: OpenFAST/openfast: v3.4.1, https://doi.org/10.5281/zenodo.7632918, 2023.

Jonkman, B. J.: Turbsim User's Guide: Version 1.50, https://doi.org/10.2172/965520, 2009.

Jonkman, J., Butterfield, S., Musial, W., and Scott, G.: Definition of a 5-MW Reference Wind Turbine for Offshore System Development, https://doi.org/10.2172/947422, 2009.

Kheirabadi, A. C. and Nagamune, R.: A quantitative review of wind farm control with the objective of wind farm power maximization, J. Wind Eng. Ind. Aerodyn., 192, 45–73, https://doi.org//10.1016/j.jweia.2019.06.015, 2019.

Kröger, L., Frederik, J., van Wingerden, J.-W., Peinke, J., and Hölling, M.: Generation of user defined turbulent inflow conditions by an active grid for validation experiments, J. Phys. Conf. Ser., 1037, 052 002, https://doi.org/10.1088/1742-6596/1037/5/052002, 2018.

Lignarolo, L. E. M., Ragni, D., Scarano, F., Simão Ferreira, C., and van Bussel, G. J. W.: Tip-vortex instability and turbulent mixing in wind-turbine wakes, Journal of Fluid Mechanics, 781, 467–493, https://doi.org/10.1017/jfm.2015.470, 2015.

MATLAB: version 24.1 (R2024a), https://www.mathworks.com, 2024.

Meyers, J., Bottasso, C., Dykes, K., Fleming, P., Gebraad, P., Giebel, G., Göçmen, T., and van Wingerden, J.-W.: Wind farm flow control: prospects and challenges, Wind Energy Sci., 7, 2271–2306, https://doi.org/10.5194/wes-7-2271-2022, 2022.

Munters, W. and Meyers, J.: Towards practical dynamic induction control of wind farms: analysis of optimally controlled wind-farm boundary layers and sinusoidal induction control of first-row turbines, Wind Energy Sci., 3, 409–425, https://doi.org/10.5194/wes-3-409-2018, 2018.

Neuhaus, L., Berger, F., Peinke, J., and Hölling, M.: Exploring the capabilities of active grids, Exp. Fluids, 62, 130, https://doi.org/10.1007/s00348-021-03224-5, 2021.

Neunaber, I., Hölling, M., Stevens, R. J. A. M., Schepers, G., and Peinke, J.: Distinct Turbulent Regions in the Wake of a Wind Turbine and Their Inflow-Dependent Locations: The Creation of a Wake Map, Energies, 13, https://doi.org/10.3390/en13205392, 2020.

Porté-Agel, F., Bastankhah, M., and Shamsoddin, S.: Wind-turbine and wind-farm flows: A review, Boundary Layer Meteorol., 174, 1–59, https://doi.org/10.1007/s10546-019-00473-0, 2020.

Schottler, J., Hölling, A., Peinke, J., and Hölling, M.: Design and implementation of a controllable model wind turbine for experimental studies, J. Phys. Conf. Ser., 753, 072 030, https://doi.org/10.1088/1742-6596/753/7/072030, 2016.

Taschner, E., van Vondelen, A., Verzijlbergh, R., and van Wingerden, J.: On the performance of the helix wind farm control approach in the conventionally neutral atmospheric boundary layer, Journal of Physics: Conference Series, 2505, 012 006, https://doi.org/10.1088/1742-6596/2505/1/012006, 2023.

Uluocak, S., Theuer, F., Neuhaus, L., Inestroza, M. A. Z., Hulsman, P., and Kühn, M.: The lidar probe volume averaging effect: A wind tunnel investigation in streamwise turbulence with continuous-wave lidar, Journal of Physics: Conference Series, 2767, 042 027, https://doi.org/10.1088/1742-6596/2767/4/042027, 2024.

van der Hoek, D., Kanev, S., Allin, J., Bieniek, D., and Mittelmeier, N.: Effects of axial induction control on wind farm energy production - A field test, Renewable Energy, 140, 994–1003, https://doi.org/https://doi.org/10.1016/j.renene.2019.03.117, 2019.

van der Hoek, D., Frederik, J., Huang, M., Scarano, F., Simao Ferreira, C., and van Wingerden, J.-W.: Experimental analysis of the effect of dynamic induction control on a wind turbine wake, Wind Energy Sci., 7, 1305–1320, https://doi.org/10.5194/wes-7-1305-2022, 2022.

van der Hoek, D., Ferreira, C. S., and Wingerden, J.-W. V.: Experimental comparison of induction control methods for wind farm power maximization on a scaled two-turbine setup, Journal of Physics: Conference Series, 2767, 092 064, https://doi.org/10.1088/1742-6596/2767/9/092064, 2024.

van Dooren, M. F., Campagnolo, F., Sjöholm, M., Angelou, N., Mikkelsen, T., and Kühn, M.: Demonstration and uncertainty analysis of synchronised scanning lidar measurements of 2-D velocity fields in a boundary-layer wind tunnel, Wind Energy Sci., 2, 329–341, https://doi.org/10.5194/wes-2-329-2017, 2017.

van Dooren, M. F., Kidambi Sekar, A. P., Neuhaus, L., Mikkelsen, T., Hölling, M., and Kühn, M.: Modelling the spectral shape of continuous-wave lidar measurements in a turbulent wind tunnel, Atmospheric Measurement Techniques, 15, 1355–1372, https://doi.org/10.5194/amt-15-1355-2022, 2022.

van Wingerden, J. W., Fleming, P. A., Göçmen, T., Eguinoa, I., Doekemeijer, B. M., Dykes, K., Lawson, M., Simley, E., King, J., Astrain, D., Iribas, M., Bottasso, C. L., Meyers, J., Raach, S., Kölle, K., and Giebel, G.: Expert Elicitation on Wind Farm Control, J. Phys. Conf. Ser., 1618, 022 025, https://doi.org/10.1088/1742-6596/1618/2/022025, 2020.

Wagner, R., Courtney, M., Gottschall, J., and Lindelöw-Marsden, P.: Accounting for the speed shear in wind turbine power performance measurement, Wind Energy, 14, 993–1004, https://doi.org/https://doi.org/10.1002/we.509, 2011.

Wang, C., Campagnolo, F., Sharma, A., and Bottasso, C. L.: Effects of dynamic induction control on power and loads, by LES-ALM simulations and wind tunnel experiments, J. Phys. Conf. Ser., 1618, 022 036, https://doi.org/10.1088/1742-6596/1618/2/022036, 2020.

Wang, C., Campagnolo, F., Canet, H., Barreiro, D. J., and Bottasso, C. L.: How realistic are the wakes of scaled wind turbine models?, Wind Energy Science, 6, 961–981, https://doi.org/10.5194/wes-6-961-2021, 2021.

Yılmaz, A. E. and Meyers, J.: Optimal dynamic induction control of a pair of inline wind turbines, Phys. Fluids, 30, 085 106, https://doi.org/10.1063/1.5038600, 2018.

Zúñiga Inestroza, M. A., Hulsman, P., and Petrović, V.: On the impact of different static induction control strategies on a wind turbine wake, J. Phys. Conf. Ser., 2767, 092 082, https://doi.org/10.1088/1742-6596/2767/9/092082, 2024.

Zúñiga Inestroza, M. A., Hulsman, P., Petrović, V., and Kühn, M.: Data Supplement for ’Dynamic induction control for mitigation of wake-induced power losses: a wind tunnel study under different inflow conditions’, https://doi.org/10.5281/zenodo.15356141, 2025.